Roles of MKI67, GNL2, and MDN1 in Chromosome Organization, Nucleolar Function, and Transcriptome Regulation

Shiro Iuchi * and Joao A. Paulo

Department of Cell Biology
Harvard Medical School, 240 Longwood Ave., Boston, MA, 02115, USA

*To whom correspondence should be addressed. Email: iuchiss@hotmail.com

ABSTRACT

The MGM complex, comprising the MKI67 (Ki-67), GNL2, and MDN1 proteins, plays a crucial role in RNA metabolism. However, the functions of these proteins are largely unknown. Here, we describe their functions. MKI67 binds to proliferating-cell chromosomes through consensus sequences and primarily localizes at the nucleolar periphery. Peripheral MKI67 maintains pre-60S particles in the nucleolus and then releases them into the nucleus by recruiting MDN1 via GNL2. This MKI67 also appears to be essential for importing nucleolar proteins and protein complexes. Furthermore, it is associated with organizing acrocentric and non-acrocentric chromosomes. Additionally, MKI67 regulates the levels of numerous genomic transcripts, including UNC13A and NEK7. MKI67 downregulates UNC13A during transcription and downregulates NEK7 by involving mRNA degradation systems. MKI67 knockdown upregulates SLC7A2 transcripts and its paralogs. These transcripts are known to activate mTORC1 and increase protein synthesis and proliferation. This finding implies that the absence of MKI67 enables differentiated tissue cells to live longer and perform their cell-type-specific activities. MDN1 knockdown downregulates the pre-60S particle-related RNAs and respiratory complex transcripts. This indicates the existence of a mechanism that prevents wasteful energy production when ribosome biosynthesis decreases. Collectively, MKI67, GNL2, and MDN1 regulate chromosome organization, nucleolar function, and transcriptomes.

INTRODUCTION

Proteins in cells often work together within large complexes, such as ribosomes, spliceosomes, transcriptomes, and the CCR4-NOT complex (1-4). Each of these complexes carries out a biosynthetic or biodegradative process. However, we recently revealed that these complexes are interconnected, forming the "RNAmetasome network", which coordinates the regulation of these processes (5). The MGM complex, consisting of MKI67, GNL2, and MDN1 on chromosomes, appears to be at the core of this network. Building on our previous research, this study reveals that the MGM complex is essential for exporting pre-60S particles from the nucleolus to the nucleus. Additionally, this study suggests that MKI67 imports proteins with a nucleolar localization signal (NoLS) and their RNA complexes. MKI67 is also involved in arranging the distribution of chromosomes around the periphery. Furthermore, this study reveals that these proteins regulate the levels of genomic RNA transcripts. For example, knockdown of MKI67 increases the levels of numerous transcripts, including cell-type-specific mRNA and mRNA that activates the mechanistic target of rapamycin complex 1 (mTORC1), which activates anabolic processes and proliferation(6). On the other hand, knockdown of MDN1 strongly decreases transcripts involved in pre-60S particle processing and respiratory complex formation. This finging suggests the presence of a coordinated regulatory system between ribosome biogenesis and its energy supply system.

MKI67 was initially identified by Gerdes and his colleagues as a marker present exclusively in dividing cells of human tissues (7,8). This discovery led to the development of a valuable diagnostic tool for cancer. However, recent studies have shown that MKI67 is not essential for cell proliferation (5,9,10). These findings have raised the fundamental question of MKI67's role in human cells. What does MKI67 do in human cells? MKI67 exists in two forms. The longer version contains 3,256 amino acids. The shorter version contains 2,896 amino acids and lacks a segment yet retains its main features (7,11,12). MKI67 has numerous regions consisting of

charged amino acid residues, resulting in many intrinsically disordered regions (IDRs) throughout the molecule (Figure 1A). These regions allow MKI67 to extend within cells (13,14). Its N-terminus contains an FHA domain to which NIFK binds (15), and its C-terminus has a 321-residue domain that preferentially binds to AT-rich DNA sequences. This preference was identified by comparing the competitive inhibition strength of alternating copolymer DNAs against a mixed ligands that bind to the 321-residue DNA-binding domain (16). Between these two ends, MKI67 contains a PP1 motif, to which the PP1γ phosphatase binds (17,18), as well as 16 tandem repeats of 122 residues each (Schluter et al., 1993). MKI67 is typically located at the periphery of the nucleolus and is associated with heterochromatin rather than rRNA transcription sites (10,19-23). These findings suggest that MKI67 does not directly regulate rRNA genes, but rather, it silences other genomic genes through heterochromatin. During mitosis, MKI67 coats the chromosomes with a thick peri-chromosomal layer (PCL). This layer forms through the activity of the C-terminal region and central repeats, which are stimulated by CDK-1-driven phosphorylation (12,17,24,25). The PCL acts as a surfactant, keeping sister chromatids apart so they can separate correctly (14). During anaphase, MKI67 is dephosphorylated by PP1γ (18). MKI67's transcription is tightly regulated (26). The DREAM complex, which consists of MuvB and its repressor subunits, binds to both repressive and activating cis elements. This binding mode represses MKI67 transcription in G0/G1. Later, however, MuvB replaces these subunits with proteins such as B-MYB. This results in binding only to the activating cis element, leading to transcription activation, which peaks in prophase and mitosis (26-28). Tumor suppressors p53/p21 also indirectly suppress MKI67. Interestingly, cells experience mitotic DNA damage in the absence of MKI67, and this damage is more severe when p53 is also absent. The C-terminal DNA-binding domain can reverse this issue, highlighting its role in maintaining genome stability (9).

Ribosome biogenesis begins in the nucleolus, where the 45S precursor ribosomal RNA (pre-rRNA) is transcribed from the rRNA genes located in the nucleolar organizing regions (NORs) on chromosomes 13, 14, 15, 21, and 22. In contrast, the 5S rRNA is produced on chromosome 1 and imported into the nucleolus. Many other proteins, RNAs, and ribonucleoproteins (RNPs) are also imported to the nucleolus, where they play a role in processing the pre-ribosome particles. For example, small nucleolar RNAs (snoRNAs) are crucial for covalently modifying RNAs, including pre-rRNA (29). The modified rRNAs acquire a specific structure, which is necessary for being cleavage into smaller pieces, 5.8S and 38S precursors. XRN2 exonuclease trims these precursors to create 5.8S and 38S rRNAs, respectively. These rRNAs remain in the pre-60S particles (1,30-34). The RIX1 complex (PELP1, NOL9, TEX10, WDR18, and SENP3) and many other factors are recruited to the pre-60S particles. MDN1, an AAA-ATPase (Figure 1C), is also recruited and plays a crucial role in processing the pre-60S particles. SUMOylated PELP1 is responsible for this recruitment (35). In S. cerevisiae, the Rea1 homolog of MDN1 moves with the pre-60S particle from the nucleus to the cytoplasm (1,36). The RIX1 complexes containing MDN1 in human and S. pombe cells have been found to be involved in gene silencing through heterochromatin and are called rixosomes (37,38).

GNL2 is a 731-residue GTPase that enters the nucleolus in two steps using signals present at both ends (Figure 1B). The N-terminus contains an NLS, and the C-terminus contains two NoLSs (39-41). The yeast homolog Nog2 binds to the pre-60S particles, forming the nucleolar Nog2 particles. These particles then convert to the Rix1-Real particle in the nucleus. Real replaces Nog2 with the export adaptor Nmd3, forming a complex that exits the nucleus and enters the cytoplasm. Eventually, the complex matures in the cytoplasm (1,36). In human cells,

the 60S particles are exported to the cytoplasm via Exportin 5 (42). Thus, the mechanism by which the pre-60S particles are exported from the nucleolus to the nucleus is unknown in both yeast and human cells.

MATERIALS AND METHODS

Cell culture

The HEK293T cell line (ATCC CRL-3216) was cultivated in DMEM (Thermo Fisher Scientific) supplemented with 10% fetal bovine serum (HyClone). The cultivation and the handling procedures of this cell line have been approved by the Harvard University Committee on Microbiological Safety (ID: 20-155). All experiments were conducted in accordance with the NIH rDNA Guidelines and the Federal Occupational Safety and Health Administration Bloodborne Pathogen Standard Guidelines. HEK293T cells overexpressing the *MKI67* (*Ki67*) transcripts were established by selecting cells resistant to 0.5 µg/ml puromycin after transfecting the cells with the EGFP-Ki67 plasmid, and the control cells were established using the EGFP plasmid. The EGFP-Ki67 plasmid was constructed by removing the mCherry gene from the EGFP-Ki67-mCherry plasmid (14) with BamHI-HF and NotI-HF, followed by filling and ligation (Supplementary Table 1A). Similarly, the EGFP plasmid was constructed, by digesting the original plasmid with BsrGI-HF and NotI-HF to remove the Ki67 and mCherry genes.

Cloning of the *GNL2* cDNA and its truncation

Total RNA was purified from HEK293T cultures, and the first-strand cDNA was synthesized from 600 ng of the total RNA using the ProtoScript II Kit (NEB, E6560S). Subsequently, the cDNA encoding GNL2 (Q13823) was amplified using Q5 Hot Start High-Fidelity DNA Polymerase (NEB, M0494S) and cloned into the ECORI-SCAII site of pEGFP-C2, yielding pGNL2-G7 (Supplementary Table 1A). This plasmid encodes GNL2 tagged with two tags with an N-terminal EGFP tag and a C-terminal 6x His tag. The 6x His tag was then removed, yielding pGNL2-#1. Subsequently, the two plasmids encoding full-length GNL2 were differentially truncated using the Q5 Site-Directed Mutagenesis Kit (NEB). Similarly, pGNL2-G7 and the fragments were ligated to pGEX-5X-1 at the ECORI-XhoI site to yield bacterial expression plasmids. All oligonucleotides used for cloning, truncation, and related plasmid construction were purchased from IDT (Supplementary Table 1A).

Knockdown (KD) of genes

The HEK293T culture was transfected with gene-specific DsiRNA (Dicer-substrate small interfering RNA for gene knockdown, IDT) at 40 nM concentration according to the reverse transfection protocol of Lipofectamine RNAiMAX (ThermoFisher) to knockdown the MKI67, GNL2, MDN1, YTHDC2, CNOT1, G3BP1, G3BP2, and FMR1 genes. Similarly, the HEK293T culture was transfected with a universal negative control RNA (NC1) to create the control KD cultures. For an experiment, a set of the transfected cultures was harvested after an incubation period ranging from 65 to 70 h to avoid harvesting the saturated cultures. The cells were predominantly cultured in 12-well plates, but they were also cultured in 35-mm Matsunami glass-bottom dishes for cytological work. The DsiRNAs used in this study were purchased from IDT (Supplementary Table 2).

Western blot for analysis of the cellular interaction between GNL2 and endogenous MKI67 or MDN1, as well as for analysis of gene knockdown

To investigate the native protein-protein interactions, HEK293T cells grown in a 10-cm dish were transfected with 10 µg of a plasmid encoding either full-length GNL2 or its truncated

protein using X-tremeGENE 9 DNA transfection reagent (Sigma). The cultures were cultured for two days. Nuclear extracts were prepared using the nuclear extraction buffers supplemented with 10 µM BTZ (Bortezomib, AdipoGen LIFE SCIENCES, AG-CR1-3602), after the cells were exposed to a hypotonic buffer as previously described (5). The nuclear extracts (300 µl) were precleared with a mixture of 20 µl of protein A magnetic beads and protein G magnetic beads for 60 min. The precleared nuclear extracts were then incubated with 3 µg of either rabbit anti-GFP antibody or mouse anti-6xHis antibody for 60 min. They were then incubated for 70 min after adding 20 µl of a mixture of protein A and protein G magnetic beads. The beads were washed 4 times with 300 µl of the nuclear extraction buffer containing 10 µM BTZ, suspended in 30 µl of 1.5x loading buffer. and finally heated at 100C for 5 min. Subsequently, 10 µl of the supernatant was applied to one well of 4–20% Mini-PROTEAN TGX gels (BIO-RAD, 4561096) for electrophoresis. The immunoprecipitants separated on the gel were transferred to a PVDF membrane. The proteins on the membrane were then detected using antibodies at the concentrations described in Supplementary Table 3. To investigate the effect of gene KD, KD cultures were trypsinized and collected in 1.5-ml centrifuge tubes and washed twice with PBS/1x Complete EDTA-free protease inhibitor cocktail (Roche). The cell pellets were resuspended in 30 µl of hypotonic lysis buffer, kept on ice for 20 min and subjected to two freeze-thaw cycles. The resulting cell lysates were then used as cell extracts. After estimating the protein concentration using the Micro BCA kit (Fisher Scientific), 50 µg of protein was loaded into one well of 4–20% Mini-PROTEAN TGX gels (BIO-RAD 4561094). The loaded proteins were separated by PAGE and then subjected to Western blot analysis using the antibodies listed in Supplementary Table 3.

Far western for in vitro protein-protein interaction analysis

A prey sample was loaded and separated by SDS-PAGE, then transferred to a PVDF membrane. The membrane was immersed in 20 mL of a 6 M guanidine HCl solution and incubated for 10 minutes. Then, the membrane was transferred to a solution with half the concentration of guanidine HCl (43) and incubated for 10 minutes. This transfer followed by a 10-minute incubation was repeated six times to gradually decrease the guanidine concentration to less than 100 mM. The membrane was washed twice with PBS, blocked with LI-COR blocking solution for one hour, and incubated with a probe for two hours at room temperature (RT). Purified #20 or #21 was used at the concentration (1.1 x 10^6 LI-COR units) to examine their binding affinity for the prey sample. After washing the membrane in PBS/0.1% Tween 20, it was subjected to double protein staining with a combination of primary mouse and rabbit antibodies, followed by visualization with secondary antibodies (Supplementary Table 3).

Confocal microscopy

The cultures grown on Matsunami glass-bottom dishes were rinsed once with serum- and antibiotic-free DMEM and then fixed with 4% paraformaldehyde/PBS at room temperature for 10 min. Fixation was terminated with 3x PBS, followed by replacement with 1x PBS. The fixed cultures were then dehydrated sequentially with 50%, 75%, 95%, and 100% ethanol and then air-dried. Subsequently, the cells were permeabilized with 0.2% Triton X-100/PBS for 10 min and then blocked with 1x PBS/5% BSA/0.1% IGEPAL CA630 for at least 5 min. The samples were typically double-stained with mouse and rabbit primary antibodies in the blocking buffer at 4C for 16-18 h and then washed four times with the blocking buffer. For the control staining, the blocking buffer without antibodies was used. They were further stained with two different goat secondary antibodies conjugated to a dye in the blocking buffer for 1.5 h at room temperature. Then, they were washed three times and rinsed once with water and eventually air-dried. The

samples were treated with DAPI-containing Vectashield (Vector) and examined with a confocal microscope, Lucille spinning disk & FR, at the CITE at Harvard Medical School. Immunofluorescence images were acquired by capturing the emission from the excitation of the Alexa Fluor 555 (red) and Alexa Fluor 488 (green) dyes, as well as the DAPI emission. Z-plane images of a cell (or culture field) were taken every 0.2 µm. Of these images, the one cut through the center of the nucleolus was used for comparison between images of cells that were cultured under different conditions, unless otherwise noted. The acquired images were visualized by subtracting nonspecific signals derived from the control and analyzed using Fiji (44).

Probe preparation

The E. coli strain (NEB C3013) was transformed with plasmid #20, #21, or #22, and grown in 30 ml of LB containing 100 µg/mL100-µg per ml carbenicillin to an early log phase and then induced with 0.5 mM IPTG for 4 h to produce the encoded protein from the plasmid. The cells were pelleted by centrifugation and suspended in 0.3 ml of 150 mM NaCl/25 mM Na-phosphate buffer (p8.0)/2x Complete (EDTA-free)/1mM PMSF/0.5-mg/ml lysozyme, subjected to freeze-thawing once. Then, the cells were sonicated twice at 50% output power for 5 seconds using a Branson sonicator. The extract was centrifuged at 14000 rpm for 10 min. The supernatant was mixed with Triton X-100 to reach a concentration of 0.05%. Two hundred and fifty µl of the extract were mixed with an equal volume equilibration buffer (50 mM sodium phosphate/0.3 M NaCl/10 mM imidazole/0.05% Tween 20, pH 8.0). Then, the sample mixture was applied to 50 µl of washed and diluted twofold Ni-NTA magnetic agarose (Thermo Scientific 78605). Subsequently, this agarose-extract mixture was rotated at 4C for 1 h, washed four times with 250 µl of wash buffer (50 mM sodium phosphate/0.3 M NaCl/15 mM imidazole/0.05% Tween 20, pH 8.0), and then the bound probe was eluted once with 50 µl of elution buffer A (50 mM sodium phosphate/0.3 M NaCl/0.1 M imidazole, pH 8.0). The remaining probe on the beads was then eluted twice with 50 µl of elution buffer B (50 mM sodium phosphate/0.3 M NaCl/0.3 M imidazole, pH 8.0). The last two elutes were combined and used as the probe for the Western blot.

Preparation of protein samples from KD cultures

The cultures grown in 12-well plates were rinsed once with PBS, after which they were trypsinized with 500 µL of a 0.025% trypsin/0.26 mM EDTA solution for five minutes. Trypsinization was terminated by adding 500 µL of fresh medium. The cell suspensions were transferred to 1.5-ml centrifuge tubes and washed twice with 500 µL of PBS containing an EDTA-free protease inhibitor cocktail at 4 °C. The cells were resuspended in 30 µL of a hypotonic lysis buffer containing 10 mM KCl, 10 mM HEPES (pH 7.4), 0.05% IGEPAL CA-630, 0.2 mM sodium orthovanadate, 2X EDTA-free protease inhibitor cocktail, 2 µL/mL benzonase, and 2 mM $MgCl_2$. The suspensions were placed on ice for 20 minutes and then subjected to freeze-thawing twice. Cell lysates were obtained.

Protein samples for MS analysis

Each of four protein samples (approximately 100 µg protein) prepared from duplicate KD-MKI67 and duplicate KD-CTL cultures was mixed with 10-volumes of cold 10%TCA/acetone, vortexed, and placed in a -20C freezer overnight. Precipitated proteins were collected by centrifugation at 15,000 rpm for 10 min at 4C and resuspended in 10-volumes of cold acetone of the original sample, vortexed, placed on ice for 10 min, and centrifuged at 15,000 rpm for 5 min at 4C. Proteins were washed with the 10 volumes of cold methanol of the original sample and air dried for 15 min. The samples were digested in 100µL of 100 mM EPPS, pH 8.5 and at 37°C with trypsin at a 100:1 protein-to-protease ratio overnight. The samples were desalted via

StageTip, dried via vacuum centrifugation, and reconstituted in 5% acetonitrile, 5% formic acid for LC-MS/MS processing.

Mass spectrometric data collection

Mass spectrometry data were collected using a Exploris 480 mass spectrometer (Thermo Fisher Scientific, San Jose, CA) coupled with a Proxeon 1200 Liquid Chromatograph (Thermo Fisher Scientific). Peptides were separated on a 100 µm inner diameter microcapillary column packed with ~25 cm of Accucore C18 resin (2.6 µm, 150 Å, Thermo Fisher Scientific). We loaded ~1 µg onto the column.

Peptides were separated using a 90min gradient of 3 to 22% acetonitrile in 0.125% formic acid with a flow rate of 350 nL/min. The scan sequence began with an Orbitrap MS^1 spectrum with the following parameters: resolution 60,000, scan range 350−1350 Th, automatic gain control (AGC) target "standard", maximum injection time "auto", RF lens setting 50%, and centroid spectrum data type. We selected the top twenty precursors for MS^2 analysis which consisted of HCD high-energy collision dissociation with the following parameters: resolution 15,000, AGC was set at "standard", maximum injection time "auto", isolation window 1.2 Th, normalized collision energy (NCE) 28, and centroid spectrum data type. In addition, unassigned and singly charged species were excluded from MS^2 analysis and dynamic exclusion was set to 90 s. Each sample was run twice, once with a FAIMS compensation voltage (CV) set of −40/−60/−80 V, and the second with a CV set of −30/−50/−70 V. A 1 s TopSpeed cycle was used for each CV.

Mass spectrometric data analysis

Mass spectra were processed using a Comet-based in-house software pipeline. MS spectra were converted to mzXML using a modified version of ReAdW.exe. Database searching included all entries from the humanUniProt database (downloaded September 2023), which was concatenated with a reverse database composed of all protein sequences in reversed order. Searches were performed using a 50-ppm precursor ion tolerance. Product ion tolerance was set to 0.03 Th. Oxidation of methionine residues (+15.9949 Da) was set as a variable modification. Peptide spectral matches (PSMs) were altered to a 1% FDR (45,46). PSM filtering was performed using a linear discriminant analysis, as described previously (47), while considering the following parameters: XCorr, ΔCn, missed cleavages, peptide length, charge state, and precursor mass accuracy. Peptide-spectral matches were identified, quantified, and collapsed to a 1% FDR and then further collapsed to a final protein-level FDR of 1%. Furthermore, protein assembly was guided by principles of parsimony to produce the smallest set of proteins necessary to account for all observed peptides. Spectral counts were then extracted, and the data were subsequently analyzed.

ChIP-seq

A HEK293T culture was cultivated to a density of approximately 5 x 10^7 cells in a 15-cm dish. The cells were washed once with cold PBS and then crosslinked with 300 mM EGS (Thermo Fisher Scientific) in PBS for 30 minutes. Subsequently, a second crosslinking step was performed, employing 1% formaldehyde. The crosslinking reaction was terminated by a 5-minute incubation with 125 mM glycine. Thereafter, the cells were washed and suspended in 3 ml of PBS and transferred to a centrifuge. This collection procedure was repeated to thoroughly collect the cells. The crosslinked cells were once washed with PBS, suspended in 400 µl of lysis buffer (50 mM HEPES-KOH pH8.0/140 mM NaCl/1 mM EDTA pH8/1% Triton X-100/0.1% Sodium Deoxycholate/0.5% SDS/10 µM BTZ). The cells were then placed on ice for 10 min and subsequently sonicated for 10 seconds at one-minute intervals on ice at 30% output power using a Branson sonicator. This is the general procedure for preparation of ChIP-seq samples.

However, two distinct operating conditions were employed in this study: 1) Eleven cycles of sonication were performed on 5 x 10^7 cells that had been treated with formaldehyde for 10 minutes; 2) Thirteen cycles of sonication were performed on 10 x 10^7 cells that had been treated with formaldehyde for 12 minutes. The prepared extract was diluted fivefold with dilution buffer (lysis buffer lacking SDS) and centrifuged at 14,000 rpm for 10 minutes. The resulting supernatant was precleared with a mixture of protein A and protein G magnetic beads (NEB) at 4°C for one hour. Thereafter, the supernatant was divided into four parts. Each supernatant was supplemented with 4 µg of rabbit anti-MKI67, rabbit anti-GNL2, rabbit anti-MDN1, or rabbit anti-GFP (serving as the control) and 60 µl of the protein A and protein G magnetic beads mixture. Then, they were then rotated at 4°C for 16 hours for immunoprecipitation. The beads were washed three times with 500 µl of a high-salt buffe (50mM HEPES-KOH pH 8/500 mM NaCl/1 mM EDTA/1% Triton100/0.1% SDS/0.1% Sodium Deoxycholate), washed once with 500 µL of LiCl high salt buffer (50mM HEPES-KOH pH 8/250 mM LiCl/1 mM EDTA/1% Triton100/0.1% Sodium Deoxycholate), and then suspended in 100 µl of elution buffer (50 mM Tris HCl/10 mM EDTA/1% SDS). The crosslinked DNA-protein samples were eluted by incubating the beads at 65C for 5 min, and the crosslink of the sample was removed by incubation at 65C overnight in the presence of 1 µl RNase A (20 mg/ml, NEB). Then, the proteins in the sample were digested with 2 µl proteinase K (800 u/ ml, NEB) for 1 h at 55C. Thereafter, the DNA fragments of the sample were purified using NEB PCR & DNA Cleanup Kit and dissolved in TE buffer. The concentration of the DNA fragments was determined using a Qubit fluorometer (Invitrogen). From these collected DNA fragments (20 µg), a sequencing library was prepared using the NEBNext Ultra II DNA Library Prep Kit for Illumina (NEB E7645). The library was treated with NEBNext Sample Purification Beads (E71044S) twice during the procedure, once to remove the adapter and once to clean up the end product. The High Sensitivity D1000 ScreenTape analysis showed that the end product contained DNA fragments averaging 400 bp in length with no evidence of the adapter contamination. This end-product library was subsequently sequenced to obtain 50 bp paired-end reads on an Illumina NextSeq 2000 sequencer at the Biopolymers Facilities at Harvard Medical School. The first and the second MKI67 ChIP-seq yielded 125x106 and 240x106 reads, respectively. This is consistent with the expectation resulting from the fact that these ChIP-seqs were initiated with the twofold different numbers of cells.

Statistical analysis of ChIP-seq

The quality of the sequence data was evaluated using FASTQC v0.11.9 (see FASTQC in the Data and materials availability for reference). Reads were filtered and trimmed with Atropos v1.1.31 (48) to retain high quality reads, which were then mapped to the human reference genome hg38 using Bowtie2 v2.2.5 (49). Multi-mapping reads and duplicates were removed followed by peak calling with MACS2 v2.2.7.1 (50). Likely peak artifacts were filtered out using the ENCODE blacklist (51). ChIP-seq data quality was assessed using standard ENCODE metrics, including total reads, alignment rates, fraction of reads in peaks, PCR bottleneck coefficients and the non-redundant fraction (52). Data was visualized using IGV (53). DeepTools v3.0.2 (54) was used to assess coverage and the reproducibility of peaks across replicates. ChIPseeker v1.32.0 (55) was used to annotate ChIP-seq peaks to their closest transcriptional start site and plot binding profiles. HOMER v4.11.1 (56) was used to identify enriched transcription factor binding motifs. Analyses in R were done using R v4.2.1. The MAFFT program in Lasergene 17 was used to align DNA sequences in the centromeric regions to find the long MKI67 consensus binding sequences.

RNA-seq
Triplicate cultures of KD-MKI67 and the KD-CTL were cultivated for 70 h after being transfected with 40 nM DsiRNA specific for the MKI67 gene and 40 nM negative control DsiRNA (NC1), respectively. In a separate experiment, triplicate cultures of KD-GNL2, KD-MDN1, and the KD-CTL were cultivated in the same manner after being transfected with 40 nM DsiRNA specific for the GNL2 and MDN1 genes, and 40 nM NC1, respectively. The cultures were harvested by trypsinization, and the total RNA was extracted using the Monarch Total RNA Miniprep Kit (NEB T2010S). The total RNA (1000 ng) was subjected to ribosomal RNA depletion using the NEBNext rRNA Depletion Kit v2 (E7400S), and the RNA sample was purified using NEBNext Sample Purification Beads (E7767S). The samples were fragmented by heating at 94C for 10 min. Approximately 200 bp RNA was used to synthesize indexed cDNA using the NEBNext Ultra Directional RNA Library Prep Kit for Illumina (E7765) and NEBNext Multiple Oligos for Illumina (E7335). The NEBNext RNA Sample Purification Beads (E7767S) were used for both the size selection of the adaptor-ligated DNA and cleanup of the endpoint DNA sample. High Sensitivity D1000 ScreenTape test showed that the resulting cDNA libraries contained an average DNA size of 300 bp and lacked the index primers and adapters. The library was sequenced to obtain 50 bp paired-end products on an Illumina NextSeq 500 system at the Biopolymers Facilities at Harvard Medical School. We analyzed the results using software in the RStudio software (R/4.2.1) on o2, a platform for Linux-based high-performance computing platform managed by the Research Computing Group at Harvard Medical School. The following software was used: Rhisat2 VN2.2.1 (57) to align RNA-seq reads to the reference genome (GRCh38_snp_tran/genome_snp_tran), featureCount in Rsubread V2.12.2 (58)to quantify the number of reads aligned to each gene, and DESeq2 v 1.46.0 (59) to analyze the count matrix for differential gene expression. We used Rsamtools V2.22.0 (60) to sort and index BAM files for visualization in IGV (53).

qPCR
qPCR was performed in two steps: first, first strand cDNA synthesis and second, amplification of the target cDNA. The first step was performed with the NEB LunaScript RT SuperMix Kit (E3010), and the second step was performed with the NEB Luna Universal qPCR Master Mix (M3003) using Thermo fisher Appliedbiosystems QuantStudio 7 Flex. The two-step cycling conditions recommended by NEB were employed for amplification of target and *RPS8* mRNAs. The *RPS8* was consistently expressed across a series of culture manipulations according to our RNA-seq data. Subsequently, it was used as an internal reference mRNA to calculate ΔΔCt of target mRNAs. The primers used for qPCR are listed in Supplementary Table 1B.

RESULTS AND DISCUSSION

HEK293T is a human neuronal lineage cell line
The HEK293T parent cell line, HEK293, was originally established by transforming human embryonic kidney cells with fragmented adenovirus type 5, Ad5 DNA (61). For this reason, HEK293 was traditionally considered a kidney cell line. However, subsequent research showed that Ad5 preferentially transforms neuronal cells (62), suggesting that HEK293 has a neuroectodermal origin. This idea has not yet been universally accepted. To clarify the cell origin of the HEK293T cells used in this study, we revisited and analyzed our previous mass spectrometry data using STRING within the Cytoscape platform (43,63). Out of 7,811 proteins identified, 7,570 were matched with high confidence by the database. Tissue enrichment analysis

of these transcripts revealed their predominant expression in the human nervous system, surpassing their expression in kidney or adrenal tissues (Supplementary Figure 1). Based on this evidence, we concluded that HEK293T cells originate from the neuronal lineage of the embryo. Consequently, throughout this report, we will interpret our findings as characteristic of human neuronal lineage cells.

Overall features of MKI67 binding to the chromosomes

The chromosome-MGM complex model is based on MKI67 binding to chromosomes. Therefore, we began analyzing MKI67 binding sites in biological duplicate samples. Integrative Genomic Viewer (IGV) visualizations revealed its several binding features. First, MKI67 bound to nearly the entire region of each chromosome, demonstrating consistency between the duplicate samples (Supplementary Figure 2). Second, MKI67 bound preferentially to regions with low GC content, i.e., AT-rich sequence regions. This wave-like pattern was most clearly visible on chromosomes 7 and 13 (Supplementary Figure 3). On chr13, particularly high levels of MKI67 enrichment were observed in AT-rich regions between 61 and 95 megabase pairs. Third, MKI67 barely binds to the p-arms of acrocentric chromosomes (chr13, 14, 15, 21, and 22) (Supplementary Figures 2–3). Fourth, the centromeric regions exhibited single MKI67 binding peaks, while non-centromeric regions often exhibited continuous MKI67 binding to some extent, regardless of exons or introns (Figures 1D–F). Lastly, MKI67 bound to promoter regions. However, the presence of additional MKI67 binding sites around the transcription start site (TSS) indicates that MKI67 is not a regulatory protein that functions at promoters (Figure 1G). Note that these features resulted from MKI67 binding to interphase chromosomes in non-synchronized proliferating cells, since the antibody used in this study did not virtually detect the protein during mitosis.

Nucleotide Sequences to which MKI67 binds specifically

HOMER motif discovery across the MKI67 ChIP-seq peaks identified 15 octanucleotide candidates with p-values below 1×10^{-14} (Supplementary Table 4). However, due to the unusually long DNA-binding domain of MKI67, the actual MKI67-binding DNA sequences may be longer than these octanucleotides. Consequently, to avoid identifying quasi-binding sites due to MKI67-MKI67 interaction, we searched for longer MKI67 binding sites in the centromeric regions (chr1, 2, 3, 4, 5, 7, and 13). Each centromeric peak spanned 50–120 bp of DNA (Figure 2A–F). Interestingly, however, the peak intensity greatly varied among chromosomes. The greatest binding occurred on chr7, followed by chr13, and then the others. This suggests that chr7 has the most high-quality binding sites for MKI67 binding domain. Aligning the top 65 chr7 peaks identified two longer consensus elements flanking the 5'-TGTG[ta]TGTGTG-3' motif (Figure 2G,H; Supplementary Figure 4). These consensus regions include several short motifs that are similar to the octanucleotides and often contain AT-rich sequences, such as consecutive sequences of AAA, TTT, TTTT, or an AT mixture. Sequence regions similar to the long consensus sequences appeared in the centromeric peak regions of chr13. While these two regions are not identical, they share nine to ten short motifs that maintain the spacing. In weaker binding sites on chr7 (9–11 reads), these short motifs were present in reduced numbers, indicating that a greater number of the short motifs correspond to stronger binding (Figure 2G,H). The centromeres of chromosomes 1, 2, 3, 4, and 5 lacked the long consensus motifs. To test whether these long consensus sequences also mediate MKI67 binding outside centromeres, we examined the region of chr13 (61,873,135–61,875,156), which exhibits heavy, continuous

MKI67 binding (Figure 2I). This region contained parts of consensus sequences with the correct spacing, often including AT-rich sequences (Figure 2J). Thus, these long consensus motifs can act as specific binding sites for MKI67 on chromosomes, regardless of the region. The MKI67 binding pattern on acrocentric chromosomes—pronounced on the q-arms and nearly absent on the p-arms—corresponds to the tertiary structure image: NORs localize within the nucleolus, whereas MKI67-bound regions localize on the periphery (Figure 2K) (Figure 2K) (20,22).

GNL2 and MDN1 share chromosomal binding sites with MKI67

To explore how these two proteins bind to the genome, we visualized the ChIP-seq data using BAM tracks for each protein. The initial ChIP-seq results showed that GNL2 clearly occupies the same binding sites as MKI67 (Figure 1D-1F). The results for MDN1 were initially inconclusive due to its weak reading signals. However, improvements in sample preparation amplified the MDN1 peaks, revealing that MDN1 also aligns with MKI67 binding regions. Interestingly, as MDN1 binding increased, GNL2 binding decreased. These findings suggest that these three proteins form a complex on chromosomes through a hierarchical process. First, MKI67 binds directly to DNA. Then, GNL2 binds to MKI67. Finally, MDN1 is recruited. Additionally, MKI67, GNL2, and MDN1 each bind to promoter regions in unique patterns (Figure 1G), suggesting that they bind independently to different gene promoters.

GNL2 C-termini assemble the MGM complex

The assembling order of the three proteins indicates that GNL2 plays a crucial role because its location allows it to serve as a linker between MKI67 and MDN1. To test this hypothesis, we constructed two plasmids: one encoding GNL2 tagged with EGFP at the N-terminus and 6xHis at the C-terminus (G7), and one encoding GNL2 tagged with EGFP at the N-terminus (#1). From these full-length GNL2 plasmids, we created mutants that were truncated from either the N- or C-terminus (Figure 3A). We then investigated which region of GNL2 binds to the endogenous MKI67 protein by expressing each of these proteins in HEK293T cells. Immunoprecipitation with an antibody against the tags yielded cleaved MKI67 in nuclear extracts containing full-length GNL2 but not in nuclear extracts containing the tag (#9) (Figure 3B). These results demonstrate that GNL2 binds to MKI67. GNL2 proteins truncated at the N-terminus up to residue 592 did not precipitate MKI67. However, C-terminal proteins spanning residues 593 to 731, as well as fragments of this region, precipitated MKI67. These results suggest that $GNL2^{593–731}$ or its fragments bind to MKI67. Interestingly, the 593–731 region contains many lysine and arginine residues that comprise two NoLSs and an IDR (Figures 1B and 3A). Additionally, AlphaFold 3 could not confidently define the tertiary structure of the GNL2 C-terminus or predict its interaction with MKI67(64). Nevertheless, a Far Western blot revealed that $GNL2^{643-731}$ bound to several purified MKI67 fragments (Figure 3D), while $GNL2^{593-660}$ bound weakly (See Supplementary Figure 5 for probe preparations). These results suggest that the GNL2 C-terminus binds to MKI67 via liquid-liquid phase separation (LLPS) rather than via defined domain-domain binding. Similarly, $GNL2^{643-731}$ bound to MDN1, but $GNL2^{593-660}$ did not (Figure 3E). This weaker binding to MDN1 is likely due to MDN1 having fewer IDRs than MKI67 (Figure 1A-B). During the immunoprecipitation of the full-length GNL2 using anti-tag antibodies, we found the C-terminus fragments in the precipitates in addition to the full-length GNL2 (Figure 3F). These results led us to perform an experiment whose results suggest that GNL2 forms a homocomplex through C-terminus-C-terminus binding (Figure 3G). Taken together, we conclude that MKI67 and MDN1 are linked by GNL2 C-termini via LLPS.

Using confocal microscopy, we found that a truncated version of GNL2 (#8), which retained residues 593-731 while missing residues 1-380, colocalized exactly with MKI67 at the nucleolar periphery. Truncated protein #4 ($GNL2^{1-660}$) and two full-length proteins (G7 and #1) also colocalized with MKI67. However, all three proteins were also found inside the nucleolus (Figure 3H). These results suggest that either the N-terminal region of GNL2 binds to nucleolar macromolecules or it accumulates in the nucleolus after being cleaved.

MKI67, GNL2, and MDN1 regulate the nucleolar export of the pre-60S particles at the nucleolar periphery

To determine the function of the MGM complex, we knocked down the genes that encode these proteins ((6). Knockdown of MKI67 decreased DAPI signals at the nucleolar periphery and increased them in various locations throughout the nucleus (Figure 4s A12, 4A16, 4B). Additionally, the knockdown decreased GNL2 and MDN1 levels in the nucleolus while increasing their levels in the nucleus (Figure 4s A9–A16, C, D) compared to control cultures (Figure 4s A1–A8). These results suggest that MKI67 organizes chromosomes, GNL2, and MDN1 in the nucleolus and throughout the nucleus. Conversely, knockdown of GNL2 increased nucleolar size, peripheral MKI67 levels, and nucleolar MDN1 levels (Figures 4s A17–A18, A21–A22, E, G) compared to control cultures. Similarly, knockdown of MDN1 increased nucleolar size, peripheral MKI67 levels, and nucleolar GNL2 levels (Figures 4s A25–A26, A29, A31, E, F). These results suggest that GNL2 and MDN1 are involved in peripheral MKI67 turnover. MDN1 appears to have a more direct effect than GNL2, as it is recruited to MKI67 via GNL2 last. Based on these results, we propose the following model (Figure 4H): MKI67 forms a nucleolar peripheral boundary. Immediately after forming in the nucleolus, pre-60S particles cannot diffuse across the MKI67 boundary due to its presence. However, when MDN1 is recruited via GNL2, the boundary disintegrates and release the particles to the nucleus. To validate the role of MDN1 in export, we investigated the behavior of PELP1, which is another pre-60S particle subunit that binds directly to MDN1(30,31,35). We knocked down MKI67, GNL2, and MDN1. Knockdown of MKI67 and GNL2 produced results similar to earlier observations. Compared to the controls, MKI67 knockdown increased nuclear PELP1 levels, and GNL2 knockdown increased PELP1 levels in the nucleolus (Figure 4I). Notably, MDN1 knockdown increased PELP1 levels at the nucleolar periphery while decreasing its levels in the nucleus. This result supports the model and rejects the possibility that MDN1 is involved in importing PELP1. Thus, MKI67 is essential for the nucleolar peripheral boundary, MDN1 is essential for exporting the pre-60S particles, and GNL2 is essential for recruiting MDN1 to the peripheral MKI67.

Possible function of MKI67 as a nucleolar import acceptor at the nucleolar periphery

Purified human nucleoli contain over 4,500 distinct proteins (65). Many of these proteins are expected to have one or more NoLS, while the others do not. For example, four out of six RIX1 proteins (MDN1, NOL9, SEP3, and TEX10) have two or more NoLSs whereas two other proteins (PELP1 and WDR18) lack them, according to NoD software (40,41). These two proteins lacking NoLS can enter the nucleolus by interacting with the NoLS proteins (Figure 4H1). An analysis of NoLS-containing nucleolar proteins revealed that these NoLSs consist of approximately 48% positively charged amino acids (arginine and lysine) that are not arranged in a specific order (40). This finding suggests that there is no specific nucleolar localization sequence, and that clusters of randomly linked positively charged amino acids (i.e., NoLSs) are

responsible for entering the nucleolus. GNL2 is one of these proteins and binds to the nucleolus periphery MKI67 through LLPS, as described earlier. Therefore, nucleolar proteins with NoLS motifs likely enter the nucleolus via the same mechanism as GNL2. Then, they likely migrate to their final destinations within the nucleolus, such as the NOR, due to their stronger affinity for these destinations than for MKI67. Thus, we conclude that MKI67 is essential for exporting pre-60S particles from the nucleolus and importing proteins, protein complexes, and RNA-protein complexes into the nucleolus.

Characterization of MKI67, GNL2, and MDN1 knockdown and assessment of their overall impact on downstream transcripts

As previously presented, we employed gene knockdown to analyze the function of the chromosome-MGM complex in cells. We interpreted the results based on the assumption that each knockdown would only reduce the level of its respective protein. To verify this assumption, we knocked down each gene and examined its transcript and protein levels. Each knockdown resulted in a 70–80% reduction in the target transcript level and a comparable reduction in cognate protein level (Figures 5A–5B), which aligns with our initial assumption. The only exception was the modest reduction in MDN1 protein levels due to MKI67 knockdown.

To analyze the potential downstream pathways of the MGM complex, we knocked down the MKI67, GNL2, and MDN1 genes and then performed RNA-seq. If the MGM complex always functions as a regulatory unit, knockdown of one subunit should have the same consequence as knockdown of the other two. The results were as follows: Each knockdown altered the levels of thousands of genomic transcripts, either increasing or decreasing them when applying a threshold of Padj < 0.05 (Supplementary Figure 6). Most of these transcript changes were specific to MKI67 and MDN1 knockdowns, contrary to the initial assumption (Figures 5C–5D), suggesting that MKI67 and MDN1 basically regulate transcript levels independently. For example, 86% (1,193/1,388) and 79% (1,367/1,726) of the transcripts that decreased or increased due to MKI67 knockdown, respectively, were unaffected by MDN1 knockdown. Similarly, 89% [(473–54)/473] and 71% [(560–160)/560] of the transcripts that decreased or increased due to MDN1 knockdown, respectively, were unaffected by MKI67 knockdown. One exception was similar changes between GNL2 and MDN1 knockdowns. For example, both knockdowns significantly decreased the same transcripts, including 5.8S RNAs and snoRNAs. However, the decreases were much more severe with MDN1 knockdown than with GNL2 knockdown. This finding still supports the idea that GNL2 and MDN1 independently regulate the target transcripts. Although MKI67 knockdown decreased the same transcripts, this likely occurred due to decreased MDN1 levels caused by the MKI67 knockdown. Taken together, these results suggest that MKI67, GNL2, and MDN1 independently regulate levels of genomic transcripts.

Metascape enrichment analysis (66) revealed that, based on a fold change cutoff of ≥2, transcripts belonging to the ribosome, ribosome synthesis, and spliceosome categories decreased the most in number and intensity due to the three knockdowns (Figures 5E–5G; Supplementary Tables 5–7). Conversely, transcripts that increased due to knockdown were less shared among the three knockdowns than those that decreased (Figures 5H–5J, Supplementary Tables 5–7). For example, that transcripts belonging to the neuronal system category notably increased by MKI67 knockdown, whereas those belonging to the chaperone cofactor-dependent protein refolding category increased the most by MDN1 knockdown.

Knockdown of MKI67 upregulates protein-coding transcripts via two mechanisms
Knockdown of MKI67 resulted in the upregulation of approximately 1,700 transcripts (Figures 5D). Twenty-four of these transcripts were neuron-specific and ranked among the top 55 (Supplementary Table 5). Of the 55 genes, 30 genes were found to localize to 15 heterochromatic regions and 15 to semi-heterochromatic regions, and the 17 to euchromatic regions. The remaining eight genes have not yet been mapped. The chromosomal distribution of these genes suggests that MKI67 contributes to both heterochromatin-mediated silencing and an alternative regulatory pathway. Considering the involvement of mRNA decay systems, YTHDC2 and CCR4-NOT —an idea derived from the interaction of MKI67 with YTHDC2 (5) and CCR4-NOT (Figure 6L)— we knocked down the YTHDC2 and CCR4-NOT genes and then examined the levels of NEK7 protein, whose transcript was among those increased by MKI67 knockdown. Additionally, we knocked down the stress granule component G3BP1. All of these knockdowns resulted in increased NEK7 protein levels (Figures 6A, 6H). However, these increases did not exceed those resulting from MKI67 knockdown alone (Figure 6D, 6H). These results suggest that MKI67 is essential for the activities of YTHDC2, CCR4-NOT, and G3BP1 in controlling transcript levels. For example, MKI67 forms a trafficking route to degradation systems (Figures 6M1-6M2). Unlike NEK7, knockdown of YTHDC2, CNOT1, G3BP1, or FRM1 did not increase UNC13A protein levels (Figures 7A–7E). Furthermore, contrary to the observation by RNA-seq, MKI67 knockdown did not increase UNC13A protein levels. These results raised the question of whether UNC13A transcript levels were truly upregulated by MKI67 knockdown. Consequently, we performed qPCR analysis and confirmed that the knockdown increased UNC13A transcript levels (Figures 7F-7G, Supplementary Tables 8A-B). Furthermore, hyperexpression of MKI67 decreased the high level back to nearly control levels. Therefore, we conclude that MKI67 knockdown induces high levels of UNC13A transcripts but does not increase its protein levels. Many neuronal cell transcripts are translated via a local translation mechanism (67-72). However, HEK293T cells are not neurons. This could explain why UNC13A protein levels do not increase by MKI67 knockdown. As anticipated, qPCR analysis of NEK7 transcripts revealed that their levels tended to be antiparallel to MKI67 levels (Figure 7H), which aligns with the changes in protein levels (Figure 7D, 7H). In summary, MKI67 regulates the expression of its downstream genes through two mechanisms: 1) controlling mRNA trafficking to its decay systems and 2) suppressing transcript levels during transcription.

Knockdown of MKI67 upregulates SLC7A2 transcripts that can activate mTORC1
Despite disrupting the function of the chromosome-MGM complex at the nucleolar periphery, MKI67 knockdown does not hinder proliferation or reduce rRNA levels. This cellular robustness contrasts with the G1 cell arrest caused by MDN1 or RIX1 knockdown. This difference suggests that MKI67 knockdown may induce compensatory reactions in the cells. To identify candidate genes that play such a role, we screened an RNA-seq dataset for transcripts that were up- or down-regulated by MKI67 knockdown (Figure 8A, B; Supplementary Table 9A). Several apoptosis-related genes emerged, including BNIP3 and DDIT3 (73-76). However, qPCR analysis yielded contradictory results (Figures 8E-8F, Supplementary Table 9B), suggesting that these genes do not serve as genuine survival effectors. In contrast, MKI67 knockdown upregulated SLC7A2 transcripts encoding a transporter for cationic amino acids such as L-arginine, L-lysine, and L-ornithine (Figure 8C, D); and a qPCR analysis proved that high levels of MKI67 decreases SLC7A2 transcript levels (Figure 8G, Supplementary Table 9B).

Furthermore, MKI67 knockdown upregulated its paralogs, SLC7A5 and SLC7A6 transcripts. These results suggest that low levels of MKI67, driven by MKI67 knockdown, activate mTORC1 through elevated SLC7A2 and its paralogs, resulting in increased protein synthesis and cell proliferation (6). Several reports have linked SLC7A2 hyperexpression to the enhanced proliferation of islet cells, muscle differentiation, and cancer aggressiveness (77-79). Therefore, we propose that SLC7A2-mediated mTORC1 activation counterbalances ribosomal stress and sustains continuous cell proliferation in MKI67-depleted cells (Figure 8H). Since non-dividing, differentiated cells in tissues naturally lack MKI67 (7,8), the increased SLC7A2 and its paralogs effectively preserve viability and support cell-type-specific gene and protein expression over extended lifespans—a mechanism that is particularly relevant to long-lived neurons.

Loss of MDN1 leads to downregulation of transcripts for respiration complexes

We observed an acidification in cultures knocked down for MDN1 or MKI6 but not in cultures knocked down for GNL2 or the control. Acidification began two days after the knockdown and persisted for three days (Figure 9A; Supplementary Figure 7). The MDN1 knockdown cultures exhibited the most severe acidification. Conversely, the reduction in MDN1 levels in the MKI67 knockdown cultures may have caused the acidification. Because the acidification suggests that metabolic shifts occurred in these cells, we searched for transcripts potentially involved in the pH reduction. Unexpectedly, many transcripts emerged as the candidates. For example, knockdown of MDN1 significantly decreased the mitochondrial transcripts, MT-RNR1 and MT-RNR2 (Supplementary Figure 8, Supplementary Table 7), as well as respiratory gene transcripts, including ISCA1 and CYCS (Figures 9B–9C, supplementary Table 10). These decreased transcripts may have caused pleiotropic impairments in respiration. For example, the absence of ISCA1, which is necessary for integrating iron-sulfur centers, could impair respiratory complexes I, II, III, and IV (Figures 9B–9C). Meanwhile, the transcripts of glycolytic enzymes increased slightly (Supplementary Table 10), which may contribute to culture acidification. The transcripts of the heat shock proteins HSPA1A and HSPA1B increased concomitantly, possibly in response to an increase in proteins separated from nucleoprotein complexes due to a lack of RNA. These results suggest that MDN1 plays a key role in preventing excess energy production when ribosome biogenesis, which requires a lot of energy, is low. This MDN1-mediated mechanism acts in the opposite direction of the energy-dependent nucleolar silencing complex (eNoSC), which reduces ribosome biogenesis by repressing rRNA transcription when the energy sources are scarce (e.g., when glucose levels are low) (80).

MDN1 binds nearly exclusively to the promoter regions of Pol III-dependent genes

MDN1 bound to promoter regions independently of MKI67 and GNL2. It bound to the 5' ends of protein-coding genes, such as DAB2IP, PAK4, RFX1, and SGSM1 (Supplementary Figures 9A–9B), and to the 5' ends of Pol III-dependent genes, such as the RNY1/3/4, RNU6, RMRP, and RN7SK gene (Supplementary Figures 9C–9F). However, MDN1 bound to the latter group of genes over ten times more strongly than to the former. Additionally, MDN1 could weakly bind to the 3' ends of the RNY3 and RNU6-2 genes. Extreme binding of this type occurred with the RMRP and RN7SK genes, where MDN1 covered them entirely. Nevertheless, knockdown of MDN1 did not significantly alter their transcript levels compared to other RNA gene transcripts of the same group (Supplementary Figures 9–10). These results suggest that MDN1 is not a conventional transcription factor, but rather plays a different role, such as stabilizing transcripts by forming their tertiary structures. Another possibility is that MDN1 selects Pol III over Pol II

to terminate transcription precisely at the 5' end of small target genes (2,81-83). Interestingly, although several RNU genes exist, MDN1 binds only to RNU6 genes, which encode transcripts that recruit Mg^{2+} ions and splice pre-mRNA (2). This feature may provide insight into the role of MDN1 binding to Pol III-dependent genes.
GNL2 bound to the promoter regions of several genes. However, knockdown of GNL2 caused weaker changes in transcript levels than changes in transcripts from genes to which GNL2 did not bind.

HEK293T cells as a tool to understand nerve cell-specific local translation.
In HEK293T cells, knockdown of MKI67 increased NEK7 transcript and protein levels, however, it increased UNC13A transcript levels without concomitantly increasing protein levels. This discrepancy between the UNC13A transcripts and proteins appears to result from a lack of local translation of UNC13A transcripts because HEK293T cells are not neurons. Since knockdown of MKI67 induces many neuron-specific transcripts, including UNC13A, HEK293T cells could help identify which neuron-specific transcripts undergo local translation. These results would add new members to the list of local translation transcripts and confirm existing members (67). Furthermore, research using HEK293T cells could accelerate the process of gaining insight into the local translation mechanism.

ACKNOWLEDGEMENTS

We thank Dr. Danesh Moazed for his invaluable support and mentorship. We are grateful to Dr. Steven Gygi for access to the mass spectrometry facilities, and to Drs. Lingsheng Dong, Swapnil Suresh Parhad, William G. Rodriguez, and Harleen Saini for guidance on RNA-seq statistical analysis using the o2 high-performance computing platform. We appreciate Drs. Wenzhi Feng, Redi Metali, and Shuai Sun for training on the Applied Biosystems QuantStudio 7 Flex, and the CITE at Harvard Medical School for confocal microscopy access. We also thank the Biopolymers Facility Genomics Core (RRID:SCR_007175) for next-generation sequencing and the Harvard Chan Bioinformatics Core (RRID:SCR_025373)—especially Sergey Naumenko, Noor Sohail, and Shannan Ho Sui—for assistance with ChIP-seq data analysis. Their efforts were supported in part by the Harvard Medical School Foundry.

Author contributions: SI designed the study, performed experiments, analyzed the data, and wrote the manuscript. J.A.P. conducted mass spectrometry experiments and wrote the corresponding methods section.

COMPETING INTERESTS

The authors declare no competing interests.

FUNDING

S.I. received support from the late Dr. Howard Green. J.A.P. was supported by an NIH grant (GM132129).

DATA AVAILABILITY

The plasmids utilized in this study were deposited at Addgene.
The ChIP-seq and RNA-Seq data were deposited in the Gene Expression Omnibus (GEO) database. The ChIP-seq accession number is GSE288519, and the RNA-seq accession numbers are GSE287864 and GSE287866. The MS data were deposited at Pride, and the project accession number is PXD060366.

The following websites were utilized in the present study:
NoD (Nucleolar Localization Sequence Detector) at University of Dundee:
https://www.compbio.dundee.ac.uk/www-nod/
FastQC for ChIP-seq data:
https://www.bioinformatics.babraham.ac.uk/projects/fastqc/ developed by the Bioinformatics Group at the Babraham Institute.
Gene and Protein characteristics:
https://www.ncbi.nlm.nih.gov/datasets/gene/; https://www.uniprot.org/uniprotkb
Cytoscape:
https://cytoscape.org/
Metascape:
https://metascape.org/gp/index.html#/main/step1
AlphaFold 3:
https://alphafoldserver.com/welcome

REFERENCES

1. Klinge, S. and Woolford, J.L., Jr. (2019) Ribosome assembly coming into focus. *Nature reviews. Molecular cell biology*, **20**, 116–131.
2. Wilkinson, M.E., Charenton, C. and Nagai, K. (2020) RNA Splicing by the Spliceosome. *Annual review of biochemistry*, **89**, 359–388.
3. Murakami, S. and Jaffrey, S.R. (2022) Hidden codes in mRNA: Control of gene expression by m(6)A. *Molecular cell*, **82**, 2236–2251.
4. Pavanello, L., Hall, M. and Winkler, G.S. (2023) Regulation of eukaryotic mRNA deadenylation and degradation by the Ccr4-Not complex. *Front Cell Dev Biol*, **11**, 1153624.
5. Iuchi, S. and Paulo, J.A. (2021) RNAmetasome network for macromolecule biogenesis in human cells. *Commun Biol*, **4**, 1399.
6. Chantranupong, L., Scaria, S.M., Saxton, R.A., Gygi, M.P., Shen, K., Wyant, G.A., Wang, T., Harper, J.W., Gygi, S.P. and Sabatini, D.M. (2016) The CASTOR Proteins Are Arginine Sensors for the mTORC1 Pathway. *Cell*, **165**, 153–164.
7. Gerdes, J., Schwab, U., Lemke, H. and Stein, H. (1983) Production of a mouse monoclonal antibody reactive with a human nuclear antigen associated with cell proliferation. *International journal of cancer. Journal international du cancer*, **31**, 13–20.
8. Scholzen, T. and Gerdes, J. (2000) The Ki-67 protein: from the known and the unknown. *Journal of cellular physiology*, **182**, 311–322.
9. Garwain, O., Sun, X., Iyer, D.R., Li, R., Zhu, L.J. and Kaufman, P.D. (2021) The chromatin-binding domain of Ki-67 together with p53 protects human chromosomes

from mitotic damage. *Proceedings of the National Academy of Sciences of the United States of America*, **118**.
10. Sobecki, M., Mrouj, K., Camasses, A., Parisis, N., Nicolas, E., Lleres, D., Gerbe, F., Prieto, S., Krasinska, L., David, A. *et al.* (2016) The cell proliferation antigen Ki-67 organises heterochromatin. *eLife*, **5**, e13722.
11. Gerdes, J., Li, L., Schlueter, C., Duchrow, M., Wohlenberg, C., Gerlach, C., Stahmer, I., Kloth, S., Brandt, E. and Flad, H.D. (1991) Immunobiochemical and molecular biologic characterization of the cell proliferation-associated nuclear antigen that is defined by monoclonal antibody Ki-67. *Am J Pathol*, **138**, 867–873.
12. Saiwaki, T., Kotera, I., Sasaki, M., Takagi, M. and Yoneda, Y. (2005) In vivo dynamics and kinetics of pKi-67: transition from a mobile to an immobile form at the onset of anaphase. *Experimental cell research*, **308**, 123–134.
13. Booth, D.G. and Earnshaw, W.C. (2017) Ki-67 and the Chromosome Periphery Compartment in Mitosis. *Trends in cell biology*, **27**, 906–916.
14. Cuylen, S., Blaukopf, C., Politi, A.Z., Muller-Reichert, T., Neumann, B., Poser, I., Ellenberg, J., Hyman, A.A. and Gerlich, D.W. (2016) Ki-67 acts as a biological surfactant to disperse mitotic chromosomes. *Nature*, **535**, 308–312.
15. Takagi, M., Sueishi, M., Saiwaki, T., Kametaka, A. and Yoneda, Y. (2001) A novel nucleolar protein, NIFK, interacts with the forkhead associated domain of Ki-67 antigen in mitosis. *The Journal of biological chemistry*, **276**, 25386–25391.
16. MacCallum, D.E. and Hall, P.A. (2000) The biochemical characterization of the DNA binding activity of pKi67. *J Pathol*, **191**, 286–298.
17. Booth, D.G., Takagi, M., Sanchez-Pulido, L., Petfalski, E., Vargiu, G., Samejima, K., Imamoto, N., Ponting, C.P., Tollervey, D., Earnshaw, W.C. *et al.* (2014) Ki-67 is a PP1-interacting protein that organises the mitotic chromosome periphery. *eLife*, **3**, e01641.
18. Takagi, M., Nishiyama, Y., Taguchi, A. and Imamoto, N. (2014) Ki67 antigen contributes to the timely accumulation of protein phosphatase 1gamma on anaphase chromosomes. *The Journal of biological chemistry*, **289**, 22877–22887.
19. Cheutin, T., O'Donohue, M.F., Beorchia, A., Klein, C., Kaplan, H. and Ploton, D. (2003) Three-dimensional organization of pKi-67: a comparative fluorescence and electron tomography study using FluoroNanogold. *J Histochem Cytochem*, **51**, 1411–1423.
20. Hori, Y., Engel, C. and Kobayashi, T. (2023) Regulation of ribosomal RNA gene copy number, transcription and nucleolus organization in eukaryotes. *Nature reviews. Molecular cell biology*, **24**, 414–429.
21. Kreitz, S., Fackelmayer, F.O., Gerdes, J. and Knippers, R. (2000) The proliferation-specific human Ki-67 protein is a constituent of compact chromatin. *Experimental cell research*, **261**, 284–292.
22. McStay, B. (2023) The p-Arms of Human Acrocentric Chromosomes Play by a Different Set of Rules. *Annu Rev Genomics Hum Genet*, **24**, 63–83.
23. Scholzen, T., Endl, E., Wohlenberg, C., van der Sar, S., Cowell, I.G., Gerdes, J. and Singh, P.B. (2002) The Ki-67 protein interacts with members of the heterochromatin protein 1 (HP1) family: a potential role in the regulation of higher-order chromatin structure. *J Pathol*, **196**, 135–144.
24. Hayashi, Y., Kato, K. and Kimura, K. (2017) The hierarchical structure of the perichromosomal layer comprises Ki67, ribosomal RNAs, and nucleolar proteins. *Biochemical and biophysical research communications*, **493**, 1043–1049.

25. Valverde, J.M., Dubra, G., Phillips, M., Haider, A., Elena-Real, C., Fournet, A., Alghoul, E., Chahar, D., Andres-Sanchez, N., Paloni, M. *et al.* (2023) A cyclin-dependent kinase-mediated phosphorylation switch of disordered protein condensation. *Nature communications*, **14**, 6316.
26. Uxa, S., Castillo-Binder, P., Kohler, R., Stangner, K., Muller, G.A. and Engeland, K. (2021) Ki-67 gene expression. *Cell Death Differ*, **28**, 3357–3370.
27. Gerdes, J., Lemke, H., Baisch, H., Wacker, H.H., Schwab, U. and Stein, H. (1984) Cell cycle analysis of a cell proliferation-associated human nuclear antigen defined by the monoclonal antibody Ki-67. *Journal of immunology*, **133**, 1710–1715.
28. Miller, I., Min, M., Yang, C., Tian, C., Gookin, S., Carter, D. and Spencer, S.L. (2018) Ki67 is a Graded Rather than a Binary Marker of Proliferation versus Quiescence. *Cell reports*, **24**, 1105–1112 e1105.
29. Webster, S.F. and Ghalei, H. (2023) Maturation of small nucleolar RNAs: from production to function. *RNA Biol*, **20**, 715–736.
30. Castle, C.D., Cassimere, E.K. and Denicourt, C. (2012) LAS1L interacts with the mammalian Rix1 complex to regulate ribosome biogenesis. *Molecular biology of the cell*, **23**, 716–728.
31. Castle, C.D., Cassimere, E.K., Lee, J. and Denicourt, C. (2010) Las1L is a nucleolar protein required for cell proliferation and ribosome biogenesis. *Molecular and cellular biology*, **30**, 4404–4414.
32. Finkbeiner, E., Haindl, M. and Muller, S. (2011) The SUMO system controls nucleolar partitioning of a novel mammalian ribosome biogenesis complex. *The EMBO journal*, **30**, 1067–1078.
33. Thiel, C.T., Horn, D., Zabel, B., Ekici, A.B., Salinas, K., Gebhart, E., Ruschendorf, F., Sticht, H., Spranger, J., Muller, D. *et al.* (2005) Severely incapacitating mutations in patients with extreme short stature identify RNA-processing endoribonuclease RMRP as an essential cell growth regulator. *American journal of human genetics*, **77**, 795–806.
34. Tomecki, R., Sikorski, P.J. and Zakrzewska-Placzek, M. (2017) Comparison of preribosomal RNA processing pathways in yeast, plant and human cells - focus on coordinated action of endo- and exoribonucleases. *FEBS letters*, **591**, 1801–1850.
35. Raman, N., Weir, E. and Muller, S. (2016) The AAA ATPase MDN1 Acts as a SUMO-Targeted Regulator in Mammalian Pre-ribosome Remodeling. *Molecular cell*, **64**, 607–615.
36. Matsuo, Y., Granneman, S., Thoms, M., Manikas, R.G., Tollervey, D. and Hurt, E. (2014) Coupled GTPase and remodelling ATPase activities form a checkpoint for ribosome export. *Nature*, **505**, 112–116.
37. Shipkovenska, G., Durango, A., Kalocsay, M., Gygi, S.P. and Moazed, D. (2020) A conserved RNA degradation complex required for spreading and epigenetic inheritance of heterochromatin. *eLife*, **9**.
38. Zhou, H., Stein, C.B., Shafiq, T.A., Shipkovenska, G., Kalocsay, M., Paulo, J.A., Zhang, J., Luo, Z., Gygi, S.P., Adelman, K. *et al.* (2022) Rixosomal RNA degradation contributes to silencing of Polycomb target genes. *Nature*, **604**, 167–174.
39. Chennupati, V., Datta, D., Rao, M.R., Boddapati, N., Kayasani, M., Sankaranarayanan, R., Mishra, M., Seth, P., Mani, C. and Mahalingam, S. (2011) Signals and pathways regulating nucleolar retention of novel putative nucleolar GTPase NGP-1(GNL-2). *Biochemistry*, **50**, 4521–4536.

40. Scott, M.S., Boisvert, F.M., McDowall, M.D., Lamond, A.I. and Barton, G.J. (2010) Characterization and prediction of protein nucleolar localization sequences. *Nucleic acids research*, **38**, 7388–7399.
41. Scott, M.S., Troshin, P.V. and Barton, G.J. (2011) NoD: a Nucleolar localization sequence detector for eukaryotic and viral proteins. *BMC Bioinformatics*, **12**, 317.
42. Wild, T., Horvath, P., Wyler, E., Widmann, B., Badertscher, L., Zemp, I., Kozak, K., Csucs, G., Lund, E. and Kutay, U. (2010) A protein inventory of human ribosome biogenesis reveals an essential function of exportin 5 in 60S subunit export. *PLoS Biol*, **8**, e1000522.
43. Iuchi, S. and Paulo, J.A. (2019) Lysine-specific demethylase 2A enhances binding of various nuclear factors to CpG-rich genomic DNAs by action of its CXXC-PHD domain. *Scientific reports*, **9**, 5496.
44. Schindelin, J., Arganda-Carreras, I., Frise, E., Kaynig, V., Longair, M., Pietzsch, T., Preibisch, S., Rueden, C., Saalfeld, S., Schmid, B. *et al.* (2012) Fiji: an open-source platform for biological-image analysis. *Nature methods*, **9**, 676–682.
45. Elias, J.E. and Gygi, S.P. (2007) Target-decoy search strategy for increased confidence in large-scale protein identifications by mass spectrometry. *Nature methods*, **4**, 207–214.
46. Elias, J.E. and Gygi, S.P. (2010) Target-decoy search strategy for mass spectrometry-based proteomics. *Methods in molecular biology*, **604**, 55–71.
47. Huttlin, E.L., Jedrychowski, M.P., Elias, J.E., Goswami, T., Rad, R., Beausoleil, S.A., Villen, J., Haas, W., Sowa, M.E. and Gygi, S.P. (2010) A tissue-specific atlas of mouse protein phosphorylation and expression. *Cell*, **143**, 1174–1189.
48. Didion, J.P., Martin, M. and Collins, F.S. (2017) Atropos: specific, sensitive, and speedy trimming of sequencing reads. *PeerJ*, **5**, e3720.
49. Langmead, B. and Salzberg, S.L. (2012) Fast gapped-read alignment with Bowtie 2. *Nature methods*, **9**, 357–359.
50. Zhang, Y., Liu, T., Meyer, C.A., Eeckhoute, J., Johnson, D.S., Bernstein, B.E., Nusbaum, C., Myers, R.M., Brown, M., Li, W. *et al.* (2008) Model-based analysis of ChIP-Seq (MACS). *Genome biology*, **9**, R137.
51. Amemiya, H.M., Kundaje, A. and Boyle, A.P. (2019) The ENCODE Blacklist: Identification of Problematic Regions of the Genome. *Scientific reports*, **9**, 9354.
52. Davis, C.A., Hitz, B.C., Sloan, C.A., Chan, E.T., Davidson, J.M., Gabdank, I., Hilton, J.A., Jain, K., Baymuradov, U.K., Narayanan, A.K. *et al.* (2018) The Encyclopedia of DNA elements (ENCODE): data portal update. *Nucleic acids research*, **46**, D794–D801.
53. Robinson, J.T., Thorvaldsdottir, H., Winckler, W., Guttman, M., Lander, E.S., Getz, G. and Mesirov, J.P. (2011) Integrative genomics viewer. *Nat Biotechnol*, **29**, 24–26.
54. Ramirez, F., Ryan, D.P., Gruning, B., Bhardwaj, V., Kilpert, F., Richter, A.S., Heyne, S., Dundar, F. and Manke, T. (2016) deepTools2: a next generation web server for deep-sequencing data analysis. *Nucleic acids research*, **44**, W160–165.
55. Yu, G., Wang, L.G. and He, Q.Y. (2015) ChIPseeker: an R/Bioconductor package for ChIP peak annotation, comparison and visualization. *Bioinformatics*, **31**, 2382–2383.
56. Heinz, S., Benner, C., Spann, N., Bertolino, E., Lin, Y.C., Laslo, P., Cheng, J.X., Murre, C., Singh, H. and Glass, C.K. (2010) Simple combinations of lineage-determining transcription factors prime cis-regulatory elements required for macrophage and B cell identities. *Molecular cell*, **38**, 576–589.

57. Kim, D., Langmead, B. and Salzberg, S.L. (2015) HISAT: a fast spliced aligner with low memory requirements. *Nature methods*, **12**, 357–360.
58. Liao, Y., Smyth, G.K. and Shi, W. (2014) featureCounts: an efficient general purpose program for assigning sequence reads to genomic features. *Bioinformatics*, **30**, 923–930.
59. Love, M.I., Huber, W. and Anders, S. (2014) Moderated estimation of fold change and dispersion for RNA-seq data with DESeq2. *Genome biology*, **15**, 550.
60. Li, H., Handsaker, B., Wysoker, A., Fennell, T., Ruan, J., Homer, N., Marth, G., Abecasis, G., Durbin, R. and Genome Project Data Processing, S. (2009) The Sequence Alignment/Map format and SAMtools. *Bioinformatics*, **25**, 2078–2079.
61. Graham, F.L., Smiley, J., Russell, W.C. and Nairn, R. (1977) Characteristics of a human cell line transformed by DNA from human adenovirus type 5. *J Gen Virol*, **36**, 59–74.
62. Shaw, G., Morse, S., Ararat, M. and Graham, F.L. (2002) Preferential transformation of human neuronal cells by human adenoviruses and the origin of HEK 293 cells. *FASEB J*, **16**, 869–871.
63. Shannon, P., Markiel, A., Ozier, O., Baliga, N.S., Wang, J.T., Ramage, D., Amin, N., Schwikowski, B. and Ideker, T. (2003) Cytoscape: a software environment for integrated models of biomolecular interaction networks. *Genome research*, **13**, 2498–2504.
64. Abramson, J., Adler, J., Dunger, J., Evans, R., Green, T., Pritzel, A., Ronneberger, O., Willmore, L., Ballard, A.J., Bambrick, J. *et al.* (2024) Accurate structure prediction of biomolecular interactions with AlphaFold 3. *Nature*, **630**, 493–500.
65. Ahmad, Y., Boisvert, F.M., Gregor, P., Cobley, A. and Lamond, A.I. (2009) NOPdb: Nucleolar Proteome Database--2008 update. *Nucleic acids research*, **37**, D181–184.
66. Zhou, Y., Zhou, B., Pache, L., Chang, M., Khodabakhshi, A.H., Tanaseichuk, O., Benner, C. and Chanda, S.K. (2019) Metascape provides a biologist-oriented resource for the analysis of systems-level datasets. *Nature communications*, **10**, 1523.
67. Blanco-Urrejola, M., Gaminde-Blasco, A., Gamarra, M., de la Cruz, A., Vecino, E., Alberdi, E. and Baleriola, J. (2021) RNA Localization and Local Translation in Glia in Neurological and Neurodegenerative Diseases: Lessons from Neurons. *Cells*, **10**.
68. Dar, S.A., Malla, S., Martinek, V., Payea, M.J., Lee, C.T., Martin, J., Khandeshi, A.J., Martindale, J.L., Belair, C. and Maragkakis, M. (2024) Full-length direct RNA sequencing uncovers stress granule-dependent RNA decay upon cellular stress. *eLife*, **13**.
69. Kipper, K., Mansour, A. and Pulk, A. (2022) Neuronal RNA granules are ribosome complexes stalled at the pre-translocation state. *Journal of molecular biology*, **434**, 167801.
70. Richter, J.D. and Zhao, X. (2021) The molecular biology of FMRP: new insights into fragile X syndrome. *Nat Rev Neurosci*, **22**, 209–222.
71. Sidibe, H., Dubinski, A. and Vande Velde, C. (2021) The multi-functional RNA-binding protein G3BP1 and its potential implication in neurodegenerative disease. *J Neurochem*, **157**, 944–962.
72. Willemse, S.W., Harley, P., van Eijk, R.P.A., Demaegd, K.C., Zelina, P., Pasterkamp, R.J., van Damme, P., Ingre, C., van Rheenen, W., Veldink, J.H. *et al.* (2023) UNC13A in amyotrophic lateral sclerosis: from genetic association to therapeutic target. *J Neurol Neurosurg Psychiatry*, **94**, 649–656.
73. Bensaad, K., Tsuruta, A., Selak, M.A., Vidal, M.N., Nakano, K., Bartrons, R., Gottlieb, E. and Vousden, K.H. (2006) TIGAR, a p53-inducible regulator of glycolysis and apoptosis. *Cell*, **126**, 107–120.

74. Cancer Genome Atlas Research, N. (2014) Comprehensive molecular profiling of lung adenocarcinoma. *Nature*, **511**, 543–550.
75. Czabotar, P.E. and Garcia-Saez, A.J. (2023) Mechanisms of BCL-2 family proteins in mitochondrial apoptosis. *Nature reviews. Molecular cell biology*, **24**, 732–748.
76. Diana, P. and Carvalheira, G.M.G. (2022) NIBAN1, Exploring its Roles in Cell Survival Under Stress Context. *Front Cell Dev Biol*, **10**, 867003.
77. Coate, K.C., Dai, C., Singh, A., Stanley, J., Covington, B.A., Bradley, A., Oladipupo, F., Gong, Y., Wisniewski, S., Sellick, K. *et al.* (2024) Interruption of glucagon signaling augments islet non-alpha cell proliferation in SLC7A2- and mTOR-dependent manners. *Mol Metab*, **90**, 102050.
78. Huang, T., Zhou, J., Wang, B., Wang, X., Xiao, W., Yang, M., Liu, Y., Wang, Q., Xiang, Y. and Lan, X. (2023) Integrated Amino Acids and Transcriptome Analysis Reveals Arginine Transporter SLC7A2 Is a Novel Regulator of Myogenic Differentiation. *Int J Mol Sci*, **25**.
79. Qin, H., Sun, R., Guo, X., Fang, L., Xu, M., Teng, Y., Zhen, N., Wang, A. and Liu, J. (2023) RIOK3 promotes mTORC1 activation by facilitating SLC7A2-mediated arginine uptake in pancreatic ductal adenocarcinoma. *Aging (Albany NY)*, **15**, 1039–1051.
80. Murayama, A., Ohmori, K., Fujimura, A., Minami, H., Yasuzawa-Tanaka, K., Kuroda, T., Oie, S., Daitoku, H., Okuwaki, M., Nagata, K. *et al.* (2008) Epigenetic control of rDNA loci in response to intracellular energy status. *Cell*, **133**, 627–639.
81. Dergai, O. and Hernandez, N. (2019) How to Recruit the Correct RNA Polymerase? Lessons from snRNA Genes. *Trends Genet*, **35**, 457–469.
82. Duttke, S.H. (2014) RNA polymerase III accurately initiates transcription from RNA polymerase II promoters in vitro. *The Journal of biological chemistry*, **289**, 20396–20404.
83. Lobo, S.M. and Hernandez, N. (1989) A 7 bp mutation converts a human RNA polymerase II snRNA promoter into an RNA polymerase III promoter. *Cell*, **58**, 55–67.

Graphic Abstract

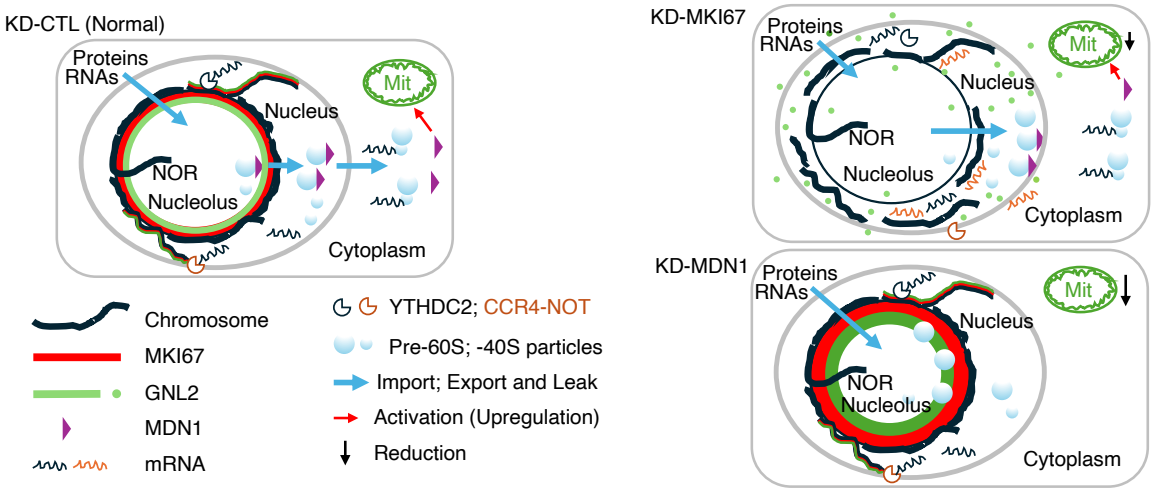

Figure 1

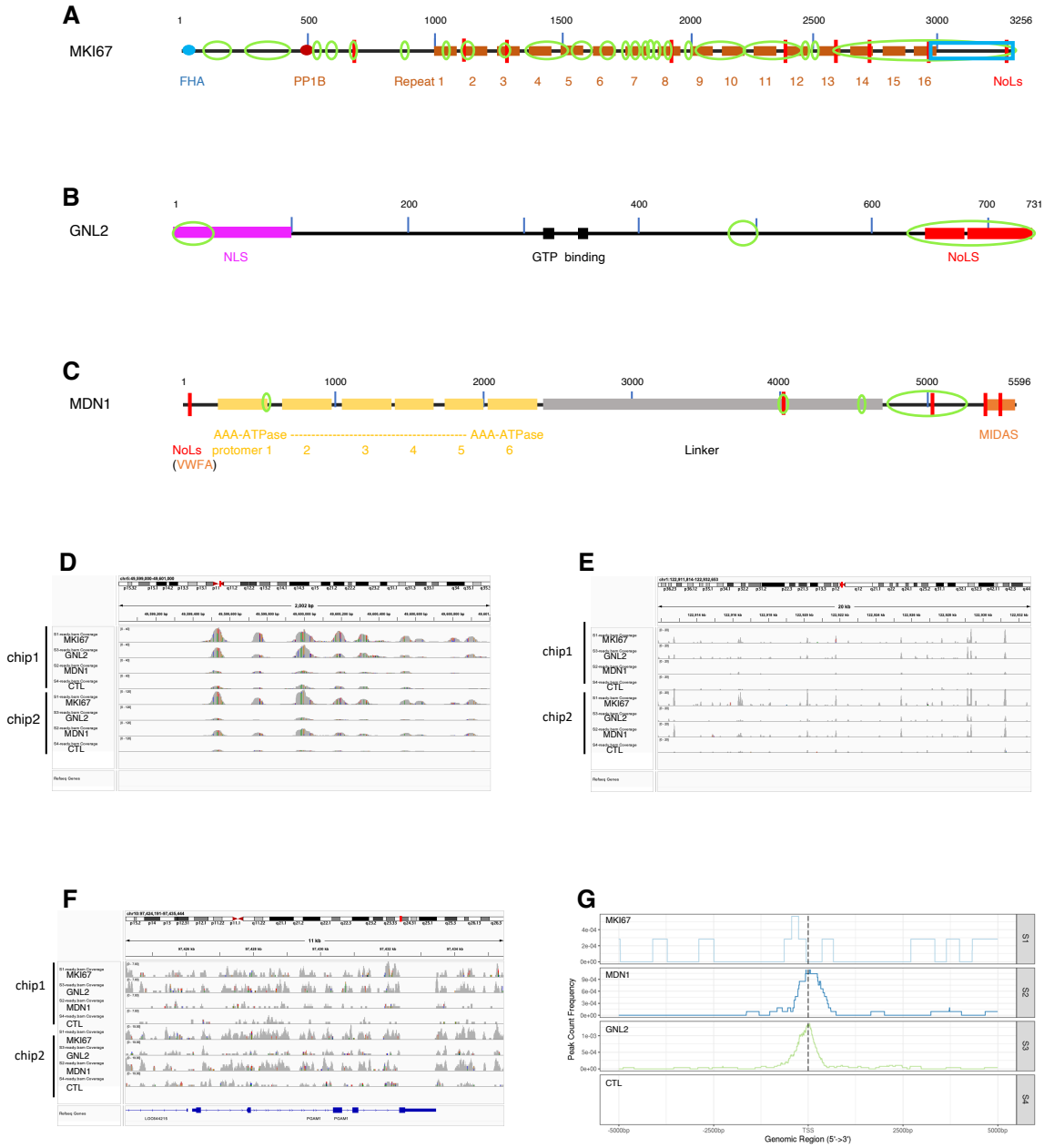

Figure 1. A-C. Schematic representations of the primary structures of proteins MKI67 (A), GNL2 (B), and MDN1 (C). The marks indicate the followings: red bar, NoLS; green loop, IDRs; blue rectangle, C-terminal DNA-binding region; and pink bar, NLS. Additional structural information is provided directly below the sketches. **D-F**. Overlap binding of MKI67, GNL2, and MDN1 at the centromeric regions of chr5 (D) and chr1 (E), as well as at the PGAM1 gene (F). **G**. Binding of MKI67, MDN1, and GNL2 at promoter regions.

Figure 2

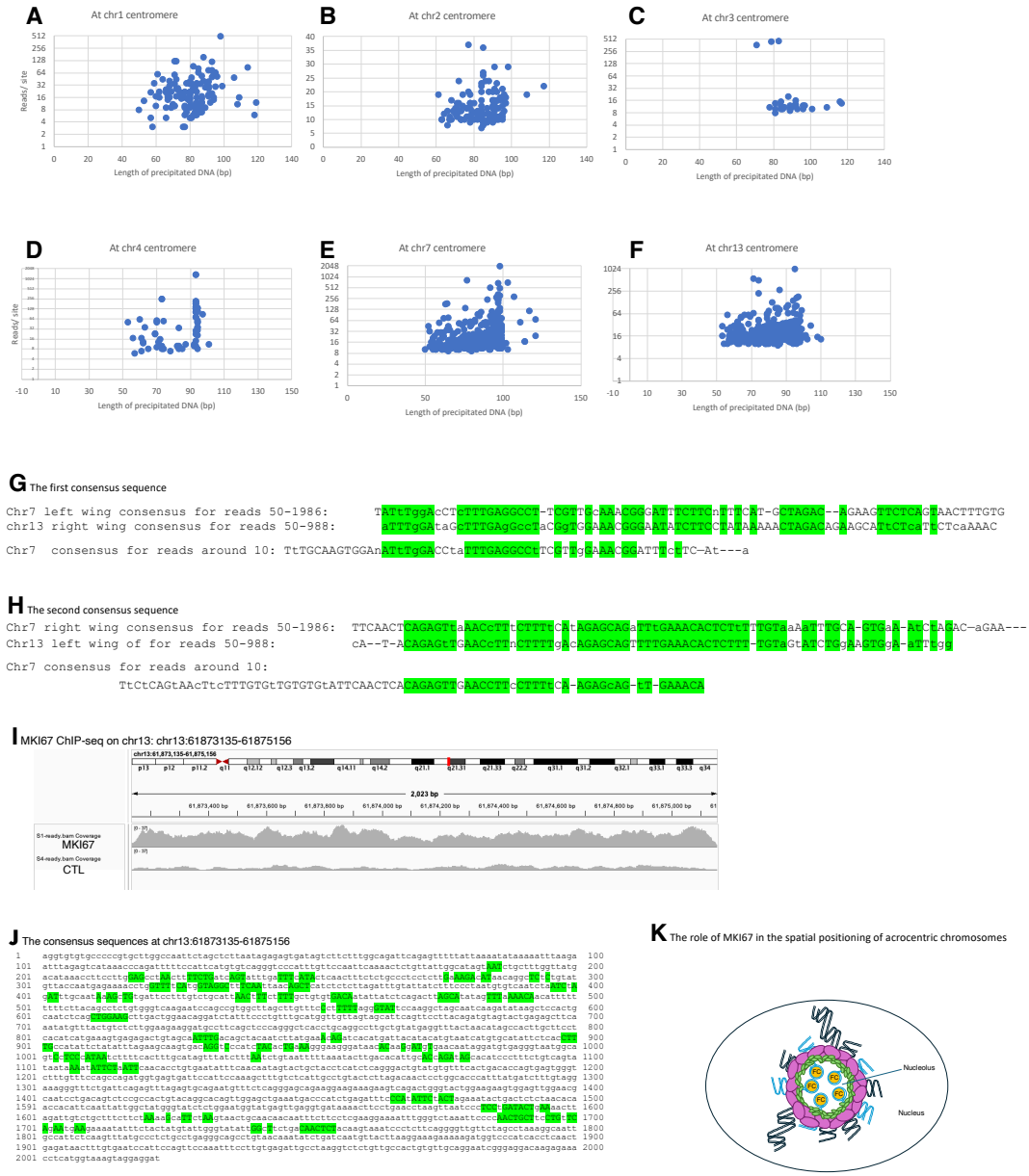

Figure 2. The details of the binding of MKI67 to chromosomes. The data presented in this figure are derived from the ChIP 2 result. **A–F**. Binding of MKI67 to the centromeric regions of chromosomes 1, 2, 3, 4, 7, and 13. The Y-axis, the total reads of the single peak area; the X-axis, the length of the nucleotide sequence to which MKI67 bound. Data with reads exceeding about eight per peak area are plotted. **G**. The first long consensus sequences to which MKI67 binds at the chr7 and chr13 centromeres. The third row displays a short consensus sequence found in the chr7 centromere. **H**. The second long consensus sequence to which MKI67 binds at the chr7 and chr13 centromeres. The third row displays a short concise consensus sequence found in the chr7 centromere. **I**. The chr13:61873135-61875156 region to which MKI67 bound most strongly along the chromosome. **J**. Consensus sequences (green) present either on the - or + strand of the chr13:61873135-61875156 region. **K**. A model of MKI67's role in the spatial positioning of acrocentric chromosomes. The blue and black drawings indicate acrocentric and non-acrocentric chromosomes, respectively. The NORs on acrocentric chromosome p-arms wrap around the FC within the nucleolus (20,22), while MKI67-bound q-arms localizes at the periphery. Red and green indicate MKI67 and GNL2, respectively.

Figure 3

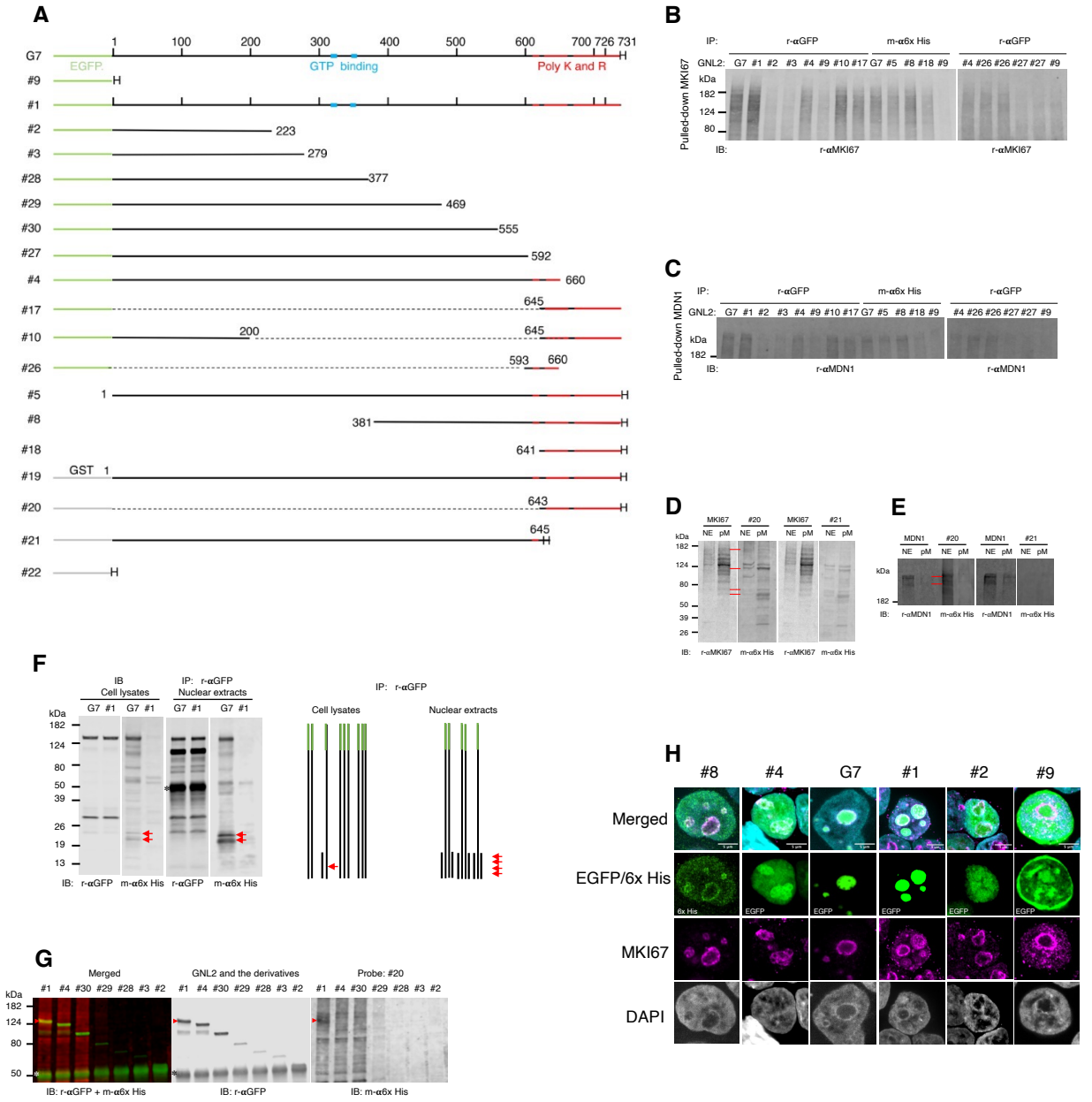

Figure 3. Binding of GNL2 to MKI67 and MDN1. **A**. Primary protein structures encoded by the cloned GNL2 and its deletion mutants. Black line, GNL2 primary structure; green line, EGFP; gray line, GST; red line, highly charged sequence regions containing lysine and arginine; H, 6xHis tag. **B**. Immunoprecipitation of the endogenous MKI67 via GNL2 and its deletion mutants. **C**. Immunoprecipitation of endogenous MDN1 via GNL2 and its deletion mutants. **D-E**. Far Western blots showing a direct binding of the C-terminus to MKI67 and MDN1. NE and pM designate lanes for nuclear extracts and purified MKI67 fragments, respectively. **F**. Binding of GNL2 C-termini to full-length GNL2. Green bar, EGFP; black star, GNL2 and its C-terminus; black star, rabbit anti-GFP antibody; red arrow, bound GNL2 C-terminus. **G**. Confirmation of the homologous C-terminus-C-terminus binding of GNL2 by Far Western blotting. GNL2 and its truncated version were expressed in HEK293T cells and immunologically purified. Then, the binding assay was performed using the C-terminus probe #20. **H**. Nucleolar periphery localization of GNL2 due to interaction between the GNL2 C-terminus and MKI67.

Figure 4

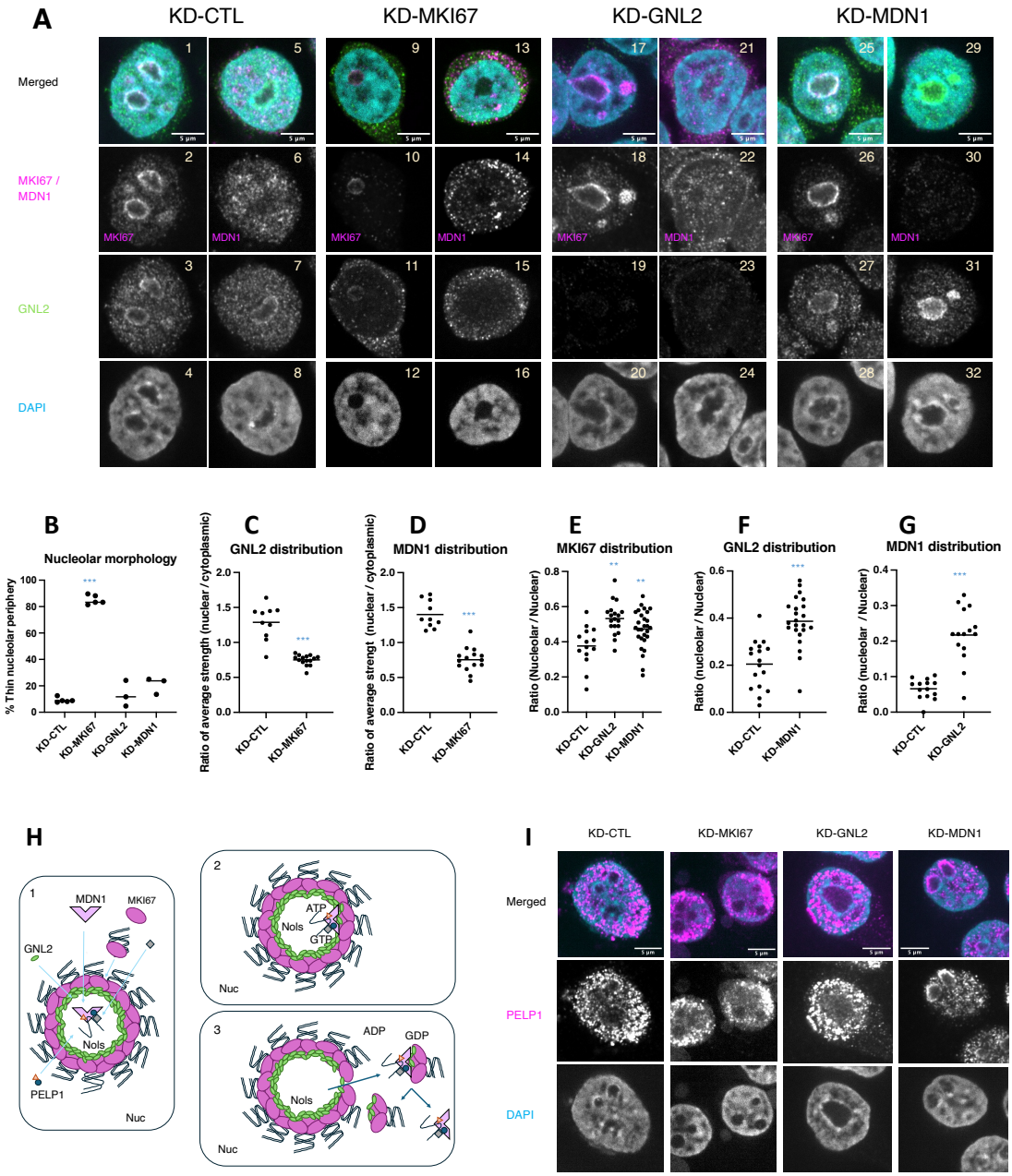

Figure 4. Function of the nucleolar periphery revealed by knockdown of MKI67, GNL2, and MDN1. **A**. Images resulting from the knockdowns. Only the merged images are displayed in color. Notes in the far-left column and on the frames of images indicate the colors used for the images. **B–G**. Results of the statistical analysis of the images in (A). T-test: **, $P < 0.001$; *** $P < 0.0001$. **H**. A model of the export of the pre-60S particle from the nucleolus to the nucleus. The nucleolus (Nols) produces pre-rRNA and imports proteins and nucleoprotein complexes through peripheral MKI67, and then they form pre-60S particles (H1). The particles are recruited to the peripheral MKI67 complex via MDN1 binding to GNL2 (H2). MDN1 then facilitates the disintegration of the peripheral MKI67 complex, releasing (exporting) the pre-60S particles into the nucleus (H3). **I**. Confirmation of the role of MDN1 in pre-60S particles. Depletion of MDN1 due to knockdown immobilizes the pre-60S particle subunit PELP1 on the nucleolar periphery. Changes in PELP1 localization due to MKI67 and GNL2 knockdowns are also shown.

Figure 5

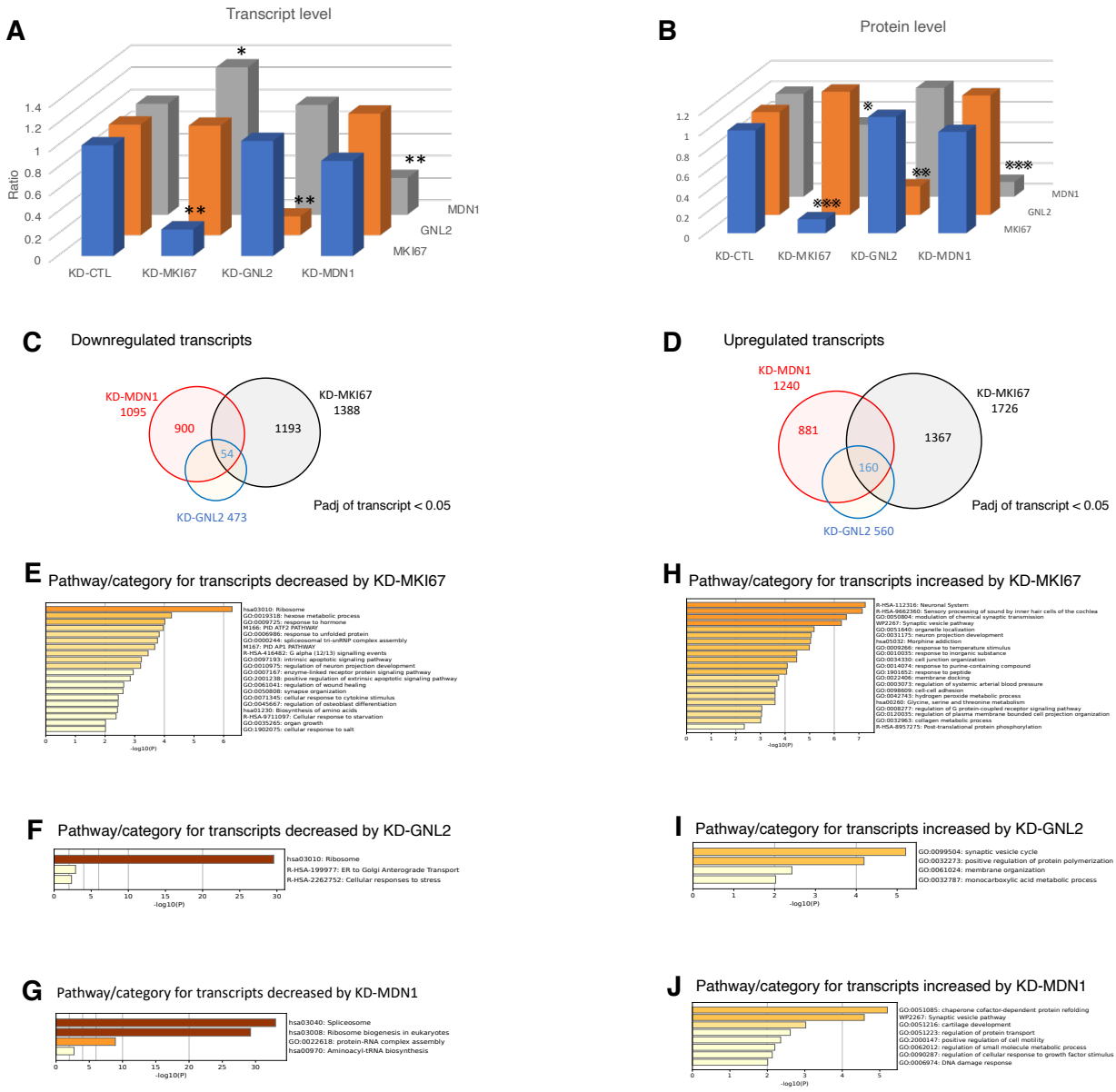

Figure 5. Knockdown of MKI67, GNL2, and MDN1 and its effect on genomic transcript levels. **A**. Levels of the MKI67, GNL2, and MDN1 transcripts following knockdown of the respective genes. These data result from the RNA-seq experiments. Each transcript level is presented as a ratio relative to that of the control culture (KD-CTL). Padj: *, <0.001; **, < 1E-37. **B**. Protein levels in the knockdown cultures. Protein levels were determined by Western blotting in four independent cultures. P-value by T-test: *, $p < 0.05$; **, $p < 0.01$; and ***, $p < 1E-05$. **C–D**. Interrelation between transcripts downregulated by MKI67, GNL2, and MDN1 depletion. **E–G**: Metascape bar graphs showing transcripts downregulated by MKI67, GNL2, and MDN1 knockdown. **H–J**: Metascape bar graphs showing transcripts upregulated by MKI67, GNL2, and MDN1 knockdown.

Figure 6

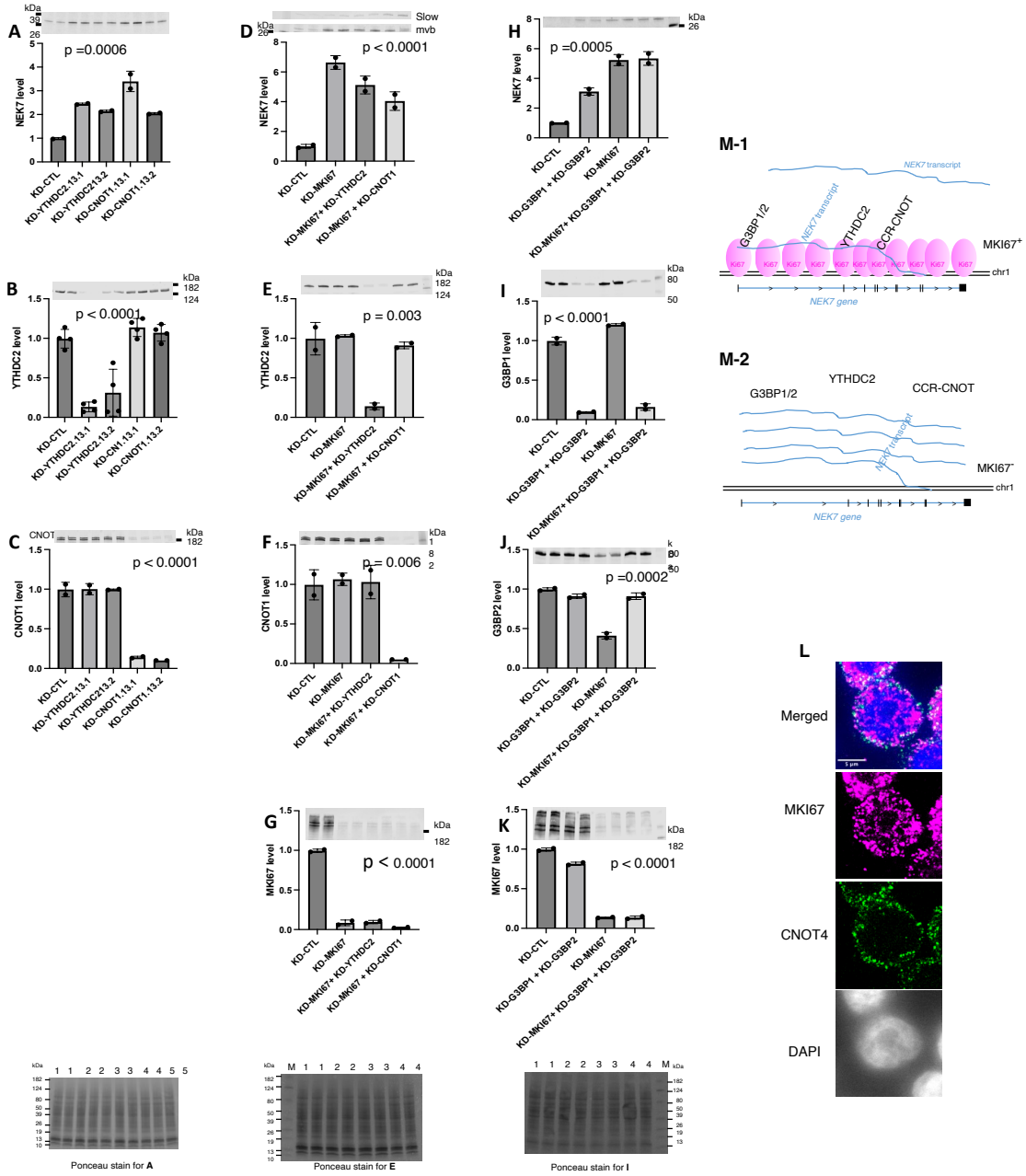

Figure 6. Upregulation of NEK7 protein levels by knockdown of YTHDC2, CNOT1, G3BP1/2, and MKI67. The statistical significance of the results was determined by conducting a one-way analysis of variance (ANOVA) test. **A**. Upregulation of NEK7 by the depletion of either YTHDC2 or CNOT1. **B–C**. Confirmation of the genes' knockdown. **D**. Knockdown of MKI67 and double knockdown of MKI67 with either YTHDC2 or CNOT1. **E–G**. Confirmation of the genes' knockdown. **H**. Upregulation of HEK7 by G3BP1 and G3BP2 knockdowns in conjunction with MKI67 knockdown. **I–K**. Confirmation of the genes' knockdown. For all Western blots, 50 µg of extract protein was added to one well of a PAGE gel. The ponceau staining image for each experiment is presented below. **L–1.** A model illustrating the degradation process of the NEK7 transcripts (blue lines). This process requires the interaction of MKI67 (pink ellipsoid) with the YTHDC2, CCR-CNOT, and G3BP1 systems. **L–2**. A model illustrating the high levels of the NEK7 transcripts due to the absence of MKI67. **M**. Colocalization of MKI67 with CNOT4 at the nuclear periphery. Images of MKI67 and CNOT4 were obtained by adjusting the Z position from the center of the nucleolus to a position where CNOT4 could be clearly observed.

Figure 7

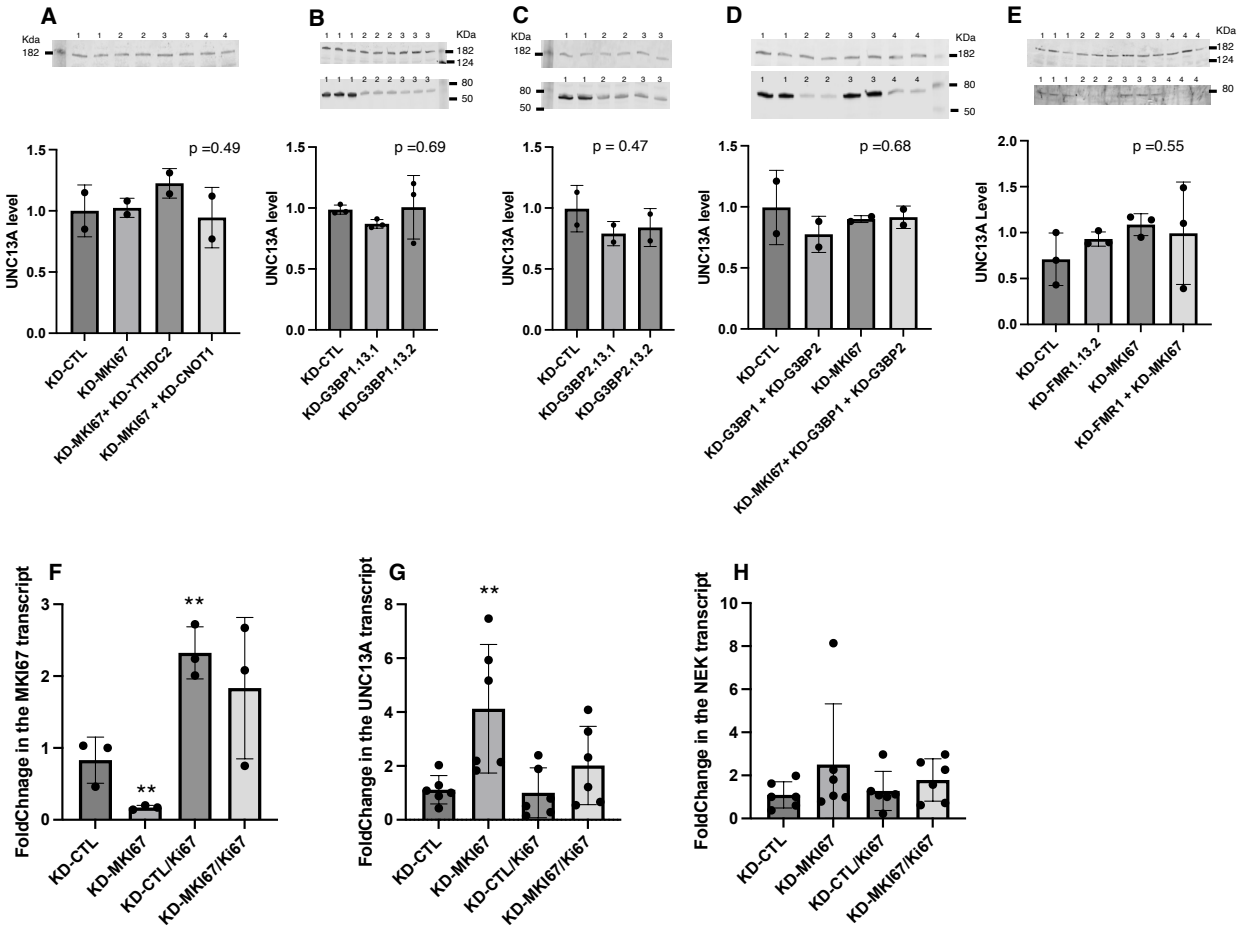

Figure 7. Gene knockdowns do not increase UNC13A protein levels. **A–E**, Knockdown of YTHDC2, CNOT1, G3BP1/2, or FRM1 does not increase UNC13A protein levels. **A, D, E**. Similarly, knockdown of MKI67 does not increase UNC13A protein levels. The upper Western blots show the UNC13A protein levels, and the lower Western blots confirm the depletion of the targeted proteins. The statistical significance of the results was determined by conducting a one-way analysis of variance (ANOVA) test. **F**. MKI67 transcript levels determined by qPCR following MKI67 knockdown, a MKI67 plasmid (Ki67) transfection, and a combination of the two. **G**. UNC13A transcript levels in the same cultures of (F). **H**. NEK7 transcript levels in the same cultures of (F). T-test: **, $p < 0.05$ compared to the control cultures (KD-CTL).

Figure 8

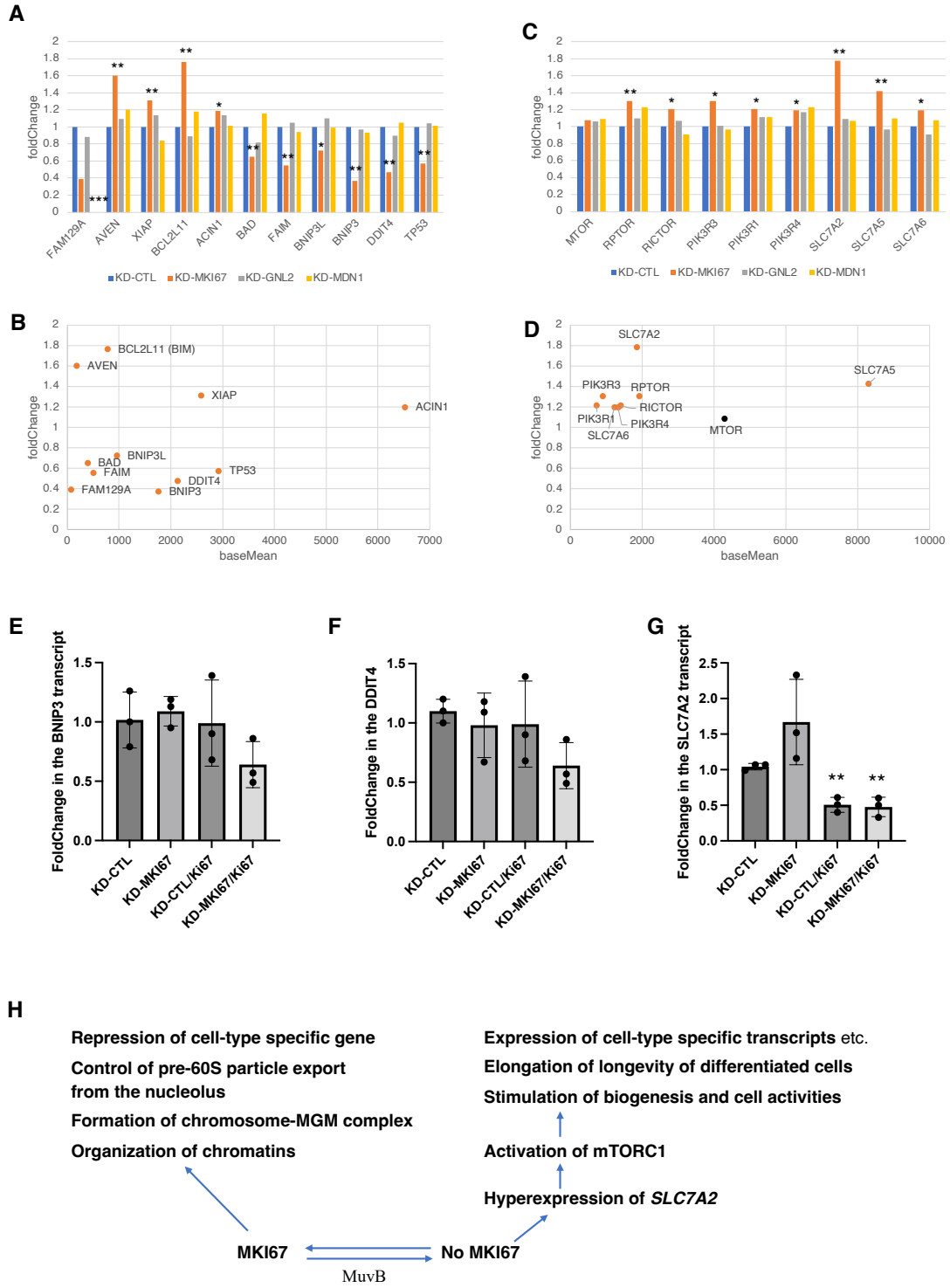

Figure 8. Roles of the presence and absence of MKI67 in regulating cellular activities. **A–B**. Apoptosis-related transcripts whose levels were altered by KD-MKI67. **C, D**. mTORC1-activating transcripts whose levels were increased by KD-MKI67. The data in panels (A–D) are derived from the RNA-seq results. Padj value: *, < 0.05; **, < 0.001. **E–G**. MKI67-dependent changes in transcripts examined by qPCR. T-test: **, p < 0.005. **H.** Overview of the MKI67 functions.

Figure 9

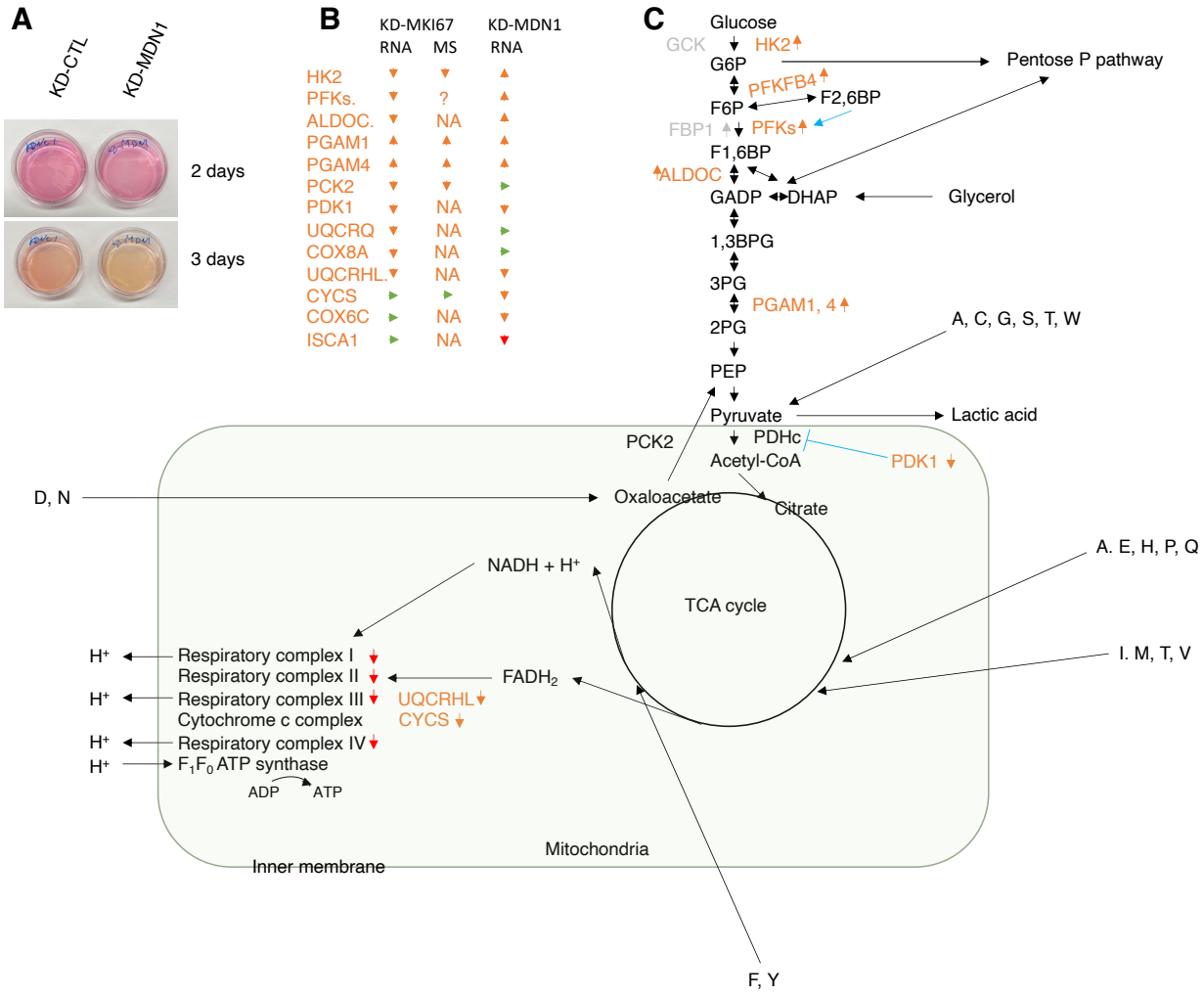

Figure 9. Metabolic shifts caused by MDN1 depletion due to knockdown. **A**. The images illustrate a decrease in pH resulting from MDN1 depletion. The cells (4x105/60-mm dish) were transfected with either hs.Ri.MDN1.13.1 or NC1 and subsequently incubated for three days. The MDN1 knockdown culture exhibited a lower pH level in compared to the control culture. **B**. Arrowheads indicate changes in expression levels obtained by RNA-seq and MS experiments: up (orange), unchanged (green), or down (orange). The "NA" indicates that the data is unavailable. **C**. Visualization of the predicted alterations in protein levels in respiration and glycolysis in MDN1-depleted cells. These alterations are based on transcript alterations obtained from the KD-MDN1 RNA-seq data. Amino acids are denoted by one-letter abbreviations. Black arrows are used to denote reaction fluxes, and blue lines indicate activation or inhibition. The red arrowhead shown adjacent to the respiration complexes signifies a predicted decrease in respiratory transport activities due to the downregulation of ISCA1 transcripts.